Elucidating the pathogenic mechanisms of AD brain-derived tau-containing extracellular vesicles: Highly transmissible and preferential propagation to GABAergic neurons

Zhi Ruan[1], Dhruba Pathak[1,2], Srinidhi-Venkatesan Kalavai[1], Asuka Yoshii-Kitahara[1], Satoshi Muraoka[1], Kayo Takamatsu-Yukawa[1], Jianqiao Hu[1], Yuzhi Wang[1], Samuel Hersh[1], Santhi Gorantla[3], Rakez Kayed[4], Howard E. Gendelman[3], Seiko Ikezu[1], Jennifer I. Luebke[2,5] and Tsuneya Ikezu[1,5, 6]

[1]Department of Pharmacology and Experimental Therapeutics, Boston University School of Medicine, Boston, MA 02118, USA; [2]Department of Anatomy and Neurobiology, Boston University School of Medicine, Boston, MA 02118, USA; [3]Department of Pharmacology and Experimental Neurosciences, University of Nebraska Medical Center, Omaha 68198, NE, USA; [4]Department of Neurology, University of Texas Medical Branch, Galveston, TX, USA; [5]Center for Systems Neuroscience, Boston University, Boston, MA 02118; [6]Department of Neurology and Alzheimer's Disease Center, Boston University School of Medicine, Boston, MA 02118, USA

Abstract

Extracellular vesicles (EVs) are highly transmissible and play critical roles in propagation of tau pathology although its mechanism remains elusive. Here, for the first time, we comprehensively characterized the pathogenic effect of human brain-derived EVs isolated from Alzheimer's disease (AD), prodromal AD (pAD) and non-demented control (CTRL) cases. AD-EVs are significantly enriched in epitope-specific tau oligomers in comparison to pAD-EVs or CTRL-EVs as determined by dot-blot and atomic force microscopy. AD-EVs were more efficiently internalized by murine cortical neurons and transferred tau, and had higher aggregation potency than pAD-EVs and CTRL-EVs *in vitro*. Strikingly, the inoculation of AD-EVs or pAD-EVs containing 300 pg of tau into the outer molecular layer of the dentate gyrus (DG) in 18 months-old C57BL/6 mice induced tau propagation throughout the hippocampus in 4.5 months, whereas inoculation of the equal amount of tau from CTRL-EV or as the oligomer or fibril-enriched fraction from the same AD donor show little propagation as determined by the semiquantitative brain-wide immunohistochemistry using multiple anti-phosphor-tau (p-tau) antibodies. AD-EVs induced accumulation of tau in the hippocampal region as both oligomers and sarkosyl-insoluble forms. Unexpectedly, p-tau^{+} cells were mostly GAD67^{+} GABAergic neurons followed by GluR2/3^{+} excitatory mossy cells, indicating preferential EV-mediated tau propagation to GABAergic neurons. Whole cell patch clamp recording of Cornu Ammonis (CA1) pyramidal cells showed significant reduction in the amplitude of inhibitory post-synaptic current. This is accompanied by the reduction in GAD67^{+}GABAergic neuronal puncta around CA1 pyramidal neurons and in c-fos^{+} GAD67^{+}GABAergic neurons in the CA1 regions, reconfirming the reduced interneuronal projections to the CA1. Our study posits a novel mechanism of brain-derived EVs in spreading pathological tau in hippocampal neurons therefore leading to their dysfunction.

Key words: Alzheimer's disease, electrophysiology, extracellular vesicle; GABAergic neuron; microtubule-associated protein tau, mouse model, tauopathy

45 **Introduction**

46 Accumulation of misfolded microtubule-associated protein tau is a neuropathological hallmark
47 of Alzheimer's disease (AD), and is closely associated with cognitive decline in AD patients [1].
48 Abnormally aggregated and phosphorylated tau (p-tau) first appear in the entorhinal cortex at the
49 prodromal stage of AD, spreading in a hierarchical pattern [1] to the hippocampal regions then
50 throughout neocortical areas [2]. A growing body of evidence suggests that the possible
51 mechanism of prion-like cell-to-cell transmission for tau propagation is as follows: extracellular
52 tau are internalized into healthy cells, where templated misfolding is induced with the
53 endogenous tau to generate into tau aggregates, leading to another cycle of tau spread by being
54 secreted from the cell. Tau is mostly secreted in free form, while a minor fraction of tau is
55 associated with extracellular vesicles (EVs) in the cerebrospinal fluid (CSF) or blood of the
56 control subjects (CTRL) and AD patients [3-7]. The levels of free tau in CSF of AD patients and
57 neuron-derived plasma EVs isolated from patients with mild cognitive impairment (MCI) or AD
58 were both correlated with the progression of disease [4, 8], suggesting potential pathogenic roles
59 of both forms of tau in disease development. It is a matter of debate, however, that EV-
60 associated and free form tau may contribute differently to tau propagation. The inoculation of
61 isolated paired helical filament (PHF)-tau from AD or other tauopathy brains were able to
62 develop tau pathology in anatomically connected regions of wild type mouse brains [9, 10]. On
63 the other hand, the inoculations of EVs isolated from transgenic tau mouse brains, human AD
64 plasma, or human induced pluripotent stem cells (iPSCs) expressing recombinant mutant tau also
65 initiated tau propagation in mouse brains [11-13]. More importantly, we and others have
66 previously shown that inhibition of exosome synthesis significantly reduced tau propagation *in*
67 *vitro* [14, 15] and *in vivo* [15]. Numerous studies have been reported for understanding the

68 mechanisms of cell-to-cell transmission of EV-associated and free form tau aggregates via their
69 secretion and uptake (for review, see [3, 16, 17]). While the mode of uptake of free tau appears
70 to be dependent on its conformational change and post-translational modifications [18-20], EV-
71 mediated tau uptake may be more influenced by the specific EV surface proteins. EVs can target
72 specific cell types by the interaction between enriched proteins on the EV surface and cell
73 surface molecules of the recipient cells [21]. To understand molecular compositions in human
74 brain-derived EVs, we have recently developed a separation protocol of human and mouse brain-
75 derived EVs, by which we successfully enriched EVs with limited contamination from cytosolic
76 components such as the endoplasmic reticulum or Golgi apparatus [22, 23]. Using this protocol,
77 we have recently reported the proteomic profiling of AD and CTRL brain-derived EVs, and
78 identified glia-derived EV molecules enriched in AD cases and significantly differentially
79 expressed proteins, which can distinguish AD from CTRL cases with 88% accuracy by a
80 machine learning approach [23]. Furthermore, our recent study on the proteomic characterization
81 of EVs isolated from interleukin (IL)-1β -stimulated human primary astrocytes have shown
82 increased expression of the integrin family, including integrin-β3 (ITGB3), which is critical for
83 neuronal EV uptake [24]. These data corroborate an idea that the disease conditions, including
84 glial inflammation, alter the molecular composition of EVs, which may modulate neuronal EV
85 uptake, therefore enhancing their potency of tau pathology spread.
86 There has been no comprehensive analysis of tau pathology development after the injection of
87 human brain-derived EVs from CTRL or AD cases. Moreover, to understand the particular
88 mechanism of EV mediated tau propagation, it is essential to assess propagation potency of EV-
89 associated and vesicle free tau isolated from the same donor. Here we aimed to characterize
90 brain-derived EVs separated from AD, prodromal AD (pAD) and age/sex-matched non-

91 demented control subjects (CTRL) for their biophysical, biochemical, and neurobiological
92 properties *in vitro*, as well as their potency for tau pathology development after their
93 intrahippocampal injection in aged C57BL/6 (B6) mice *in vivo*. The recipient mice were tested
94 by immunohistochemical and biochemical characterization of tau accumulation in the brain. We
95 also assessed the difference in tau pathology development after intrahippocampal injections of
96 EV-, tau oligomer- and tau fibril-enriched fractions from the same AD case in aged mouse
97 brains. Finally, the hippocampal region of the recipient mice was tested by whole cell patch
98 clamp recording for the assessment of the neurophysiological alteration by the tau accumulation.
99

100 **Results**

101 **Detection of tau oligomers in AD and pAD brain-derived EVs**

102 EVs consist of cell-derived lipid bilayer and are often classified as exosomes, which are 30-
103 150nm in size and are secreted after the fusion of endosomes with cell surface, and
104 microvesicles, which are 100-1000nm in size and are secreted by outward budding of plasma
105 membranes [16, 25-27]. They were originally thought to be part of the clearance system of the
106 unmetabolized cellular compositions, although accumulative evidence suggests that EVs may
107 play critical roles for spreading pathological proteins, therefore contributing to
108 neurodegenerative diseases [15, 28-30]. While tau was found both in exosomes and
109 microvesicles isolated from various tauopathy mouse brains, neuroblastoma cells, CSF, and
110 plasma in AD patients [4, 6, 7, 31], there has been no study reporting the detailed analysis of AD
111 brain-derived EVs. We first isolated exosome-enriched EV fractions from AD, pAD, and CTRL
112 patient brain samples using the previously published protocol (Supplementary Table S1 for
113 patients' demographics) [22, 23]. Briefly, the fresh-frozen post mortem brain tissues containing

114 the gray matter were lightly minced followed by the sequential centrifugations and discontinuous
115 sucrose density gradient ultracentrifugation (Fig. 1a). Analyses of the isolated fractions by the
116 transmission electron microscopy (TEM, Fig. 1b) and nanoparticles tracking analysis (NTA, Fig.
117 1c) demonstrated enrichment of EVs from these brain tissues with a size corresponding to
118 exosomes [32]. There was no difference in terms of EV particle concentration or size among the
119 three groups (Fig. 1d-e). ELISA analysis of total tau, Aβ40, and Aβ42 in EVs show abundance
120 of total tau but little detection of Aβ40 in EVs of all groups, whereas Aβ42 are enriched in AD-
121 EVs (Supplementary Table S2). Considering that tau oligomer is in the nanometer size [33], we
122 postulated that brain-derived EVs contain tau mostly in oligomer forms. Indeed, there was a
123 significantly higher amount of oligomeric tau in EVs derived from AD when compared to CTRL
124 as detected by tau oligomer-specific monoclonal antibodies TOMA-1 and TOMA-2, but not by
125 TOMA-3 or TOMA-4 (Fig. 1f-I and Supplementary Fig. S1). There was no difference in the
126 form recognized by tau oligomer polyclonal antibodies T22 and T18 among three groups (Fig.
127 1f-k). In addition, the atomic force microscopy (AFM) analysis of detergent-insoluble fraction of
128 AD-EVs and pAD-EVs, but not of CRTL-EVs, detected mostly globular particles at the mode
129 height 4-6nm, which is consistent with tau oligomers (Fig. 1l-m). Taken together, these data
130 suggest that AD-EVs and pAD-EVs are enriched in tau oligomers compared to CTRL-EVs,
131 indicating the tau seeding potency of EVs and their pathogenic roles.
132
133 **AD brain-derived EVs show efficient uptake by primary cultured neurons and subsequent**
134 **tau transfer**
135 Numerous mechanisms of EV uptake have been proposed including endocytosis,
136 macropinocytosis, phagocytosis, caveolae-dependent, clathrin-dependent, lipid raft-dependent

137 endocytosis and membrane fusion [21]. Protein-protein interaction between EVs and cell surface
138 molecules on the recipient cells can facilitate the binding of EVs and subsequent endocytosis
139 [21, 34]. For example, interaction between the integrin family on EVs and intercellular adhesion
140 molecules (ICAMs) [35] or extracellular matrix, including fibronectin and laminin, on the
141 recipient cell surface are known to be important for EV binding [21, 36, 37]. Furthermore,
142 heparin sulfate proteoglycan (HSPG) [38] and galectin [39] can mediate EV uptake. We
143 hypothesized that EV uptake differs dependent on the disease condition, which may alter
144 molecular complex on EV surface. We tested EVs isolated from human brains for their uptake by
145 primary cultured murine neurons *in vitro*. After seven days of neuronal differentiation *in vitro*,
146 the cells were incubated with PKH26-labeled EVs containing tau isolated from the brain tissue of
147 AD, pAD and CTRL samples (AD-EV tau, pAD-EV tau, and CTRL-EV tau) for 24 hours and
148 examined for the EV uptake as previously described [24] (Fig. 2a). The neuronal EV uptake was
149 significantly higher in AD-EVs compared to CTRL-EVs, while the neuronal uptake of pAD-EVs
150 was similar to CTRL-EVs (Fig. 2b-c). Concomitantly, the transfer efficiency of tau from EVs to
151 neurons normalized by the original tau input was significantly higher in AD-EVs as compared to
152 CTRL-EVs (Fig. 2d). As a negative control, we labeled the supernatant from the last
153 ultracentrifugation wash-step of the EV isolation from the brain tissue with PKH26 and applied it
154 to neuronal cells in parallel, which did not induce PKH26 positivity in neurons (data not shown),
155 confirming that the observed PKH26 positivity in neuronal cells was not due to artifacts. EV
156 surface protein repertoires are known to reflect their biological condition and cell-type specificity
157 of parental cells [21, 40]. Our recent proteome of human brain-derived EVs revealed that CTRL-
158 EVs expressed more protein of neuronal origin while AD-EVs showed more glial dominance,
159 possibly reflecting the neuroinflammatory condition, which was recently described as the third

160 core AD pathogenesis following Aβ plaques and neurofibrillary tangles (NFTs) [41]. Thus,
161 these results demonstrated that AD-EV tau are more efficiently transferred to recipient neurons
162 than CTRL- or pAD-EV tau via enhanced EV uptake, suggesting that selective AD-EV surface
163 molecules may pathologically facilitate the docking of EVs to the recipient cells. Finally, to
164 understand if EV-tau has different tau seeding activity dependent on the disease conditions, we
165 employed a FRET sensor-based tau seeding assay as previously described [42]. Astonishingly,
166 the AD-EVs showed significantly higher seeding activity compared to pAD and CTR-EVs group
167 (Fig. 2e), suggesting AD-EV possess higher potency for inducing tau pathology. In summary,
168 these data demonstrate pathogenic functions of AD-EVs, which gave us a rationale to investigate
169 tau propagation via brain-derived EVs *in vivo*.
170
171 **Inoculation of AD-EVs or pAD-EVs propagate tau pathology in aged B6 mice**
172 Since we observed efficient EV uptake and transfer of EV-tau into primary mouse cortical
173 neurons and significant tau seeding activities in AD-EVs, we further tested whether EVs isolated
174 from the human brain can initiate tauopathy in 2 months-old B6 male and female mice after an
175 intrahippocampal injection. Human brain-derived EVs (containing 300 pg tau/ injectate) isolated
176 from the brain tissue of CTRL, pAD, and AD cases were unilaterally injected into the outer
177 molecular layer (OML) of the dentate gyrus (DG) (Fig. 3a). The concentration of tau (300 pg/μl)
178 in the prepared EV sample was set in the range of the estimated physiological extracellular tau
179 concentration in the human interstitial fluid of the central nervous system [43], and is much
180 lower than the amount used for the previous tau propagation studies (1-8 μg / injectate) [9, 10].
181 Immunofluorescence against phosphorylated tau (p-tau) antibody AT8 (pSer202/pSer205)
182 detected a considerable, yet not an abundant, amount of $AT8^{+}$ cells in the hippocampal region of

183 pAD-EV or AD-EV injected female mice (Supplemental Fig. S2, left) but not in male mice (data
184 not shown). A previous study reported that a more enhanced tau propagation induced by fibril
185 tau injection was observed with aged B6 mice in comparison to young mice [9]. Therefore, we
186 decided to use aged female mice as recipients to determine if human brain-derived EVs
187 propagate tau pathology in the way reflecting the donor's disease conditions. Human brain-
188 derived EVs were isolated from 2 donors of each AD, pAD, and CTRL cases and from *Mapt*
189 knockout (Tau KO) mice as the control. Each EV sample (containing 300 pg tau/injectate for
190 human brain derived-EVs), using saline as an injection control, were unilaterally injected into the
191 OML of the DG of ~18-months-old B6 female mice (Fig. 3a). The degree of tau pathology
192 spread was evaluated by the immunofluorescence against AT8 in the hippocampal area at 4.5
193 months post injection (Fig. 3b, Supplementary Fig. S2, right, and S3a). Interestingly, abundant
194 perikaryal $AT8^+$ inclusions were detected in both ipsilateral and contralateral sides of the
195 hippocampal region including the cornus Ammonis 1 (CA1), CA3, dentate granular cells,
196 subgranular zone, and hilus in the AD and p-AD EV groups, suggesting tau transfer between
197 anatomically connected pathways (Fig. 3b). Semiquantitative brain-wide mapping of tau
198 pathologies showed that $AT8^+$ pathogenic tau was accumulated throughout the hippocampus,
199 predominantly distributed in the caudal hippocampal hilus, in the mouse brains injected with
200 AD-EVs or pAD-EVs, while CTRL-EV injected mouse brains barely showed AT8 positivity
201 (Fig. 3c). Notably, the percentage of the area occupied by $AT8^+$ cells in the hippocampal region
202 was significantly higher in AD-EV and pAD-EV groups as compared to the CTRL-EV, Saline or
203 Tau-KO-EV groups (Fig. 3c-d). There was no significant difference between Tau KO-EV and
204 CTRL-EV injected groups and no $AT8^+$ staining was observed in saline group (Fig. 3d,
205 Supplementary Fig. S3a). All $AT8^+$ neurons were negative for human tau as determined by

206 immunofluorescent staining against human tau-specific monoclonal HT7 (data not shown),
207 indicating that endogenous mouse tau was recruited and aggregated by the inoculation of human
208 EV-derived tau. A growing body of evidence suggests that misfolded tau tends to be truncated
209 and frequently consists of different conformers or structural polymorphisms, deciphering the
210 stages and disease of tauopathy [44-48]. Therefore, we performed the neuropathological analysis
211 of tau by immunohistochemistry using conformation-specific (Alz50 and MC1) and p-tau
212 epitope-specific monoclonals (CP13: pSer202 tau, PS422: pS422 tau, and PHF1:pSer396 and
213 pSer404). All 5 antibodies detected misfolded or phosphorylated tau mainly in the hilus of
214 hippocampal region with AD- and pAD-EV groups (Supplemental Fig. S3b-f).
215 We next examined whether EV-tau could induce templated misfolding of original tau aggregates
216 in endogenous tau of the recipient mice by biochemical extraction of aggregated tau from the
217 human brain-derived EV-injected mouse brains, accomplished via sarkosyl solubilization and
218 sequential centrifugation, followed by immunobloting using Tau-5 and PHF1 monoclonal
219 antibodies (Fig. 3e) as previously described [49, 50]. We observed significant increase in
220 oligomeric tau in the fraction S1p of both pAD-EV and AD-EV-injected mouse hippocampi as
221 compared to the CTRL-EV-injected group, determined by both Tau-5 (total tau) and PHF1
222 immunoblotting (Fig. 3f-g). The amount of sarkosyl-insoluble tau in the fraction P3 was also
223 significantly elevated in AD-EV-injected mouse hippocampi when compared to CTRL-EV group
224 (Fig. 3f-g). These data indicate that AD-EV inoculation induced accumulation of oligomeric and
225 fibrillar tau from an endogenous source, while pAD-EV inoculation induced accumulation of
226 oligomeric tau. Taken together, these data show the efficient induction of tau propagation in the
227 hippocampus of the aged B6 female mouse brains after the injection of the AD-EVs or pAD-EVs
228 containing physiological concentration of tau. Conformational changes of tau in the recipient

229 mice appear to reflect the original tau confirmation of AD-EVs and pAD-EVs, which were also
230 reported with mice injected with AD brain-derived tau fibrils [9].
231
232 **Inoculation of AD-EVs show more tau propagation as compared to the inoculation of an**
233 **equal amount of tau oligomer or fibril-enriched fractions from the same AD brain tissue**
234 To determine how propagation of tau pathology may differ between the injection of EV-
235 associated or free form tau, we isolated EV-, tau fibril- or tau oligomer-enriched fractions from
236 the same AD brain tissue sample, and injected each sample containing an equivalent amount of
237 tau (300pg) in 1 μL of total volume into the OML of the DG of 18-month-old B6 female mice.
238 Fibril or oligomeric tau was isolated as S1p and P3 fractions according to the previous
239 publications [9, 49, 50]. The p-tau immunoreactivity and structure of the isolated tau aggregates
240 were examined by the western blot using PHF1 antibody and AFM (Fig. 4a-b). We observed
241 mainly monomeric $PHF1^+$ band in p-tau in EV- and tau oligomer-enriched samples, and trimeric
242 $PHF1^+$ band in fibril-enriched sample (Fig. 4a). AFM images show mostly small globular
243 particles (6-8nm in height) in EV and tau oligomer preparation and large globular structures (30-
244 70nm in height), which is consistent with the description of the fibril structure as previously
245 reported [51], in sonicated tau fibril preparations (Fig. 4b). At 4.5 months after the injection,
246 mice were euthanized and tested for tau pathology by immunofluorescence against AT8. We
247 observed strong AT8 positivity in the injection site with all groups, suggesting successful
248 intrahippocampal injections. In addition, $AT8^+$ signal was also seen as perikaryal inclusions or
249 neuropil staining in the cortex along the needle tract (Supplementary Fig. S4, left), whereas only
250 neuropil accumulation of tau with oligomer or fibril tau injected mice, which is in agreement
251 with the previous study [9] (Fig. 4c, top panels, Supplementary Fig. S4, middle and right).

252 Moreover, compared to AT8^{+} tau pathology observed in the entire hippocampal region with AD-
253 EV injected mice as described previously, fibril or oligomer tau-injected mice did not show any
254 AT8^{+} perikaryal inclusions in entire hippocampus (Fig. 4c, bottom panels, d). These findings
255 recapitulated our previous study showing that inoculation of microglia-derived EVs containing
256 5ng of aggregated tau, but not the inoculation of the equal amount of free tau aggregates, was
257 able to induce tau propagation in the dentate gyrus of B6 mouse brains [15]. Previous studies
258 reported that the inoculation of 1-8 μg of fibril tau from AD patients into wildtype (B6 and
259 B6/C3H F1) mouse brains could induce tau propagation as early as 3 months post injection [9,
260 10]. Potency of propagation may be varied between the donors and the type of tauopathies [10],
261 therefore it is difficult to compare the results between these studies. To the best of our
262 knowledge, this is the first report of increased tau propagation potency in EV-tau as compared to
263 vesicle free tau isolated from the same human AD brain tissue. A previous study reported that
264 immunodepletion of tau from the AD-brain derived tau fibril diminished tau aggregation activity
265 *in vitro* or propagation *in vivo* [9]. Moreover, addition of remaining components after the
266 immunodepletion of AD-tau into fibril tau did not alter the outcome of abovementioned
267 experiments, suggesting that tau was the essential component to initiate tau propagation but not
268 tau associated molecules [9]. Our results also indicated that EVs without tau do not initiate tau
269 propagation *in vivo* as we barely observed tau propagation by injecting Tau KO-EVs. We,
270 however, confirmed that EVs certainly enhanced propagation potency of tau. The discrepancy
271 between these experiments may be due to potential removal of EVs associated with extracellular
272 tau when immunodepletion of tau was performed.
273
274 **Preferential EV-mediated tau propagation in GABAergic inhibitory neurons**

275 Recent knowledge indicates that specific type of organs or cells, where EVs are transferred,
276 could be determined by the enriched proteins on the EV surface [21]. For example, previous
277 studies found that specific EV proteins, such as integrins or tetraspanins, play critical roles for
278 the deliveries of cancer-derived EVs to specific organs or cell types [52, 53]. Given the fact that
279 some EV surface proteins are specifically expressed on AD-EVs [23], we speculated that the
280 evaluation of EV-mediated transfer of tau to aged mouse brains would uncover cell type-specific
281 tau transfer mechanisms. To determine which neuronal cell type preferentially accumulate tau,
282 we performed double immunostaining using the markers for p-tau (AT8) and GABAergic
283 interneurons (GAD67 and parvalbumin, PV) or excitatory neurons (Neurogranin, NG, and
284 glutamate receptor 2/3, GluR2/3, mossy cell marker) [54]. Surprisingly, most of $AT8^+$ cells were
285 $GAD67^+$ interneurons in the CA1, CA3, and DG region in AD-EV and pAD-EV-injected mice
286 (Fig. 5a-b). Moreover, a subset of PV^+ neurons were also co-localized with AT8 (Supplementary
287 Fig. S5a). We found that the ratio of $GAD67^+AT8^+$ cells over total $GAD67^+$ cells were
288 significantly higher in the DG region in pAD-EV and in the CA1 and CA3 region in AD-EV
289 compared to CTRL-EV injected mice (Fig. 5c-e), although there was no significant reduction in
290 the total number of $GAD67^+$ neurons in those regions. No difference was observed in any of the
291 regions between Tau KO-EV and CTRL-EV groups. In contrast, no NG^+ excitatory neurons
292 were $AT8^+$ in the DG of hippocampus (Supplementary Fig. S5b). We, however, observed that
293 some of $AT8^+$ cells were $GluR2/3^+$ mossy cells in the hilus region (Fig. 5f). Quantification of
294 $AT8^+$ cells in the hippocampal region in AD-EV injected mice revealed that 64% and 23% of the
295 $AT8^+$ cells were $GAD67^+$ inhibitory neurons and $GluR2/3^+$ excitatory mossy cells, respectively
296 (Fig. 5g). Multiple lines of evidence have supported the notion that GABAergic interneuron
297 dysfunction could be one of critical components in the early pathogenesis of AD. The decreased

298 levels of GABA transmitter have been reported in the CSF of AD patients or elderly without
299 cognitive impairment [55, 56] and in their post-mortem tissues especially in the temporal cortex,
300 followed by the hippocampus, frontal cortex, and thalamus of AD patients [57]. AD patients
301 showed loss of specific somatostatin^{+} interneurons in the hippocampus and cortex [58, 59].
302 Moreover, 7-21% of sporadic AD patients show at least one episode of seizure during the illness
303 [60], and administration of anti-epileptic drug, levetiracetam, was effective to improve cognitive
304 function in the elderly for those with normal memory, MCI, and AD patients [61, 62]. Together,
305 our data indicate that EVs may play a critical role in tau propagation of GABAergic neurons, and
306 suggest that EVs can be an attractive therapeutic target for the early intervention of AD.
307

308 **AD-EV and pAD-EV inoculation reduced GABAergic input and neuronal activity in CA1**
309 **pyramidal cells**

310 To determine if EV-mediated tau propagation may disrupt GABAergic neuronal functions, we
311 examined the number of immunostained GAD67^{+} puncta surrounding CA1 pyramidal neuronal
312 cell soma. The images were captured by confocal microscope and the number of the puncta was
313 analyzed by Imaris software (Fig. 6a). Astonishingly, there was a significant reduction in the
314 number of puncta in the CA1 pyramidal layer of pAD-EV but not AD-EV group as compared to
315 Tau KO-EV group (Fig. 6b). There was no difference between the groups in the cell numbers of
316 CA1 pyramidal neurons (Fig. 6c). We further assessed the synaptic input of GABAergic neurons
317 to CA1 pyramidal cells by examining the neuronal activity of GAD67^{+} GABAergic neurons by
318 immunofluorescence against c-fos. Strikingly, there was a significant reduction in c-fos^{+}/
319 GAD67^{+} cells in the CA1 in both AD-EV and pAD-EV as compared to Tau KO-EV injected
320 mice (Fig. 6d-e). However, there was also significant reduction in c-fos^{+}/ GAD67^{+} cells in the

321 DG in AD-EV as compared to Tau KO-EV groups (Fig. 6f-g), suggesting decreased neuronal
322 activity in GABAergic neurons specifically in the CA1 region by EV-mediated tau propagation.
323 Taken together, these data demonstrate disrupted GABAergic neuronal function by EV-mediated
324 tau propagation, which suggest CA1 pyramidal neuronal dysfunction.
325
326 **EV-induced alterations in intrinsic membrane properties and spontaneous inhibitory**
327 **synaptic currents**
328 To evaluate the effect of tau propagation in human brain-derived EV-inoculated mouse brains,
329 we performed whole-cell voltage/current–clamp recordings of CA1 pyramidal cells using 300
330 μm-thickness acute tissue slices of mouse hippocampi from Tau KO-EV, pAD-EV, and AD-EV
331 groups (Fig. 7a-b). An F-I curve-generating protocol was designed in such a way that it enables
332 us to inject a wide range of step current amplitude ranging from -100 pA to +120 pA (increment
333 of +20 pA) in High Rn protocol, while -220 pA to +330 pA (increment of +50 pA) in Low Rn
334 protocol. The number of action potentials (APs) was significantly lower in pAD-EV and aAD-
335 EV groups compared to Tau KO-EV groups as determined by repeated measurement ANOVA
336 (Fig. 7c,e, Supplementary Table S4-5) and for pAD-EV group compared to Tau KO-EV group at
337 +100 pA (p=0.0434) and +130 pA (p=0.0445) (Fig. 7d,f). This result is consistent with our study
338 on another tau transgenic mouse model (aged rTg4510 mice expressing P301L tau), which show
339 reduction in firing in hippocampal CA1 neurons [63]. AD-EV group showed significant
340 reduction of AP amplitude as compared to Tau KO-EV group (Fig. 6g). Evaluation of the
341 properties of spontaneous inhibitory and excitatory postsynaptic potentials (sIPSCs and sEPSCs)
342 (Fig. 7h and Supplementary Table S6-7) revealed significant reduction in amplitude of sIPSCs in
343 pAD-EV group and E-I ratio of amplitude as compared to Tau KO group (Fig. 7h-i). There was

344 no difference in sEPSC properties among the 3 groups. Taken together, these data demonstrate
345 reduction in excitability of pAD-EV group, reduction of AP amplitude in AD-EV group, and
346 reduction in sIPSC amplitude in pAD-EV group, which is also reflected in the reduction in the E-
347 I ratio of sIPSC amplitude. Thus, pathogenic tau accumulation may compromise both excitatory
348 and inhibitory activity of CA1 pyramidal cells.
349

350 **Discussion**

351 The current study, for the first time, demonstrated that brain-derived EVs isolated from AD or
352 pAD cases efficiently initiated tau propagation in aged B6 mice, a phenomenon which was
353 validated by the *in vitro* evidence of the highly transmissible nature of AD-EVs with higher
354 uptake by cortical neurons and increased seeding activity as compared to CTRL-EVs. Tau
355 pathology was predominantly found in GABAergic neurons and in mossy cells in the DG to a
356 lesser extent. Whole cell patch clamp recording of CA1 pyramidal cells of recipient mice showed
357 reduced intrinsic excitability and sIPSC amplitude indicative of intrinsic dysfunction of CA1
358 pyramidal cells and reduced input from interneurons. This was accompanied with reduced
359 inhibitory synaptic and c-fos immunoreactivity in GABAergic neurons in the CA1 region. The
360 preferential EV mediated tau propagation into GABAergic neurons and their reduced function
361 posits the potential underlying mechanism in interneuron dysfunction in AD.

362 Recent advances in EV research have opened new avenues to investigate the diagnostic and
363 pathogenic roles of EVs on neurodegenerative diseases [25-27]. Accumulating evidence now
364 suggests that EVs carry pathogenic proteins, and EV-associated proteins or miRNAs predict
365 disease progressions in AD [8, 64], chronic traumatic encephalopathy [65], Parkinson disease,
366 prion disease, amyotrophic lateral sclerosis, traumatic brain injury, multiple sclerosis, and

367 Huntington disease [25, 26]. Furthermore, overexpression of the second most AD-associated
368 GWAS gene, Bridging integrator-1 (BIN1), enhanced release of tau via EVs *in vitro* and
369 exacerbated tau pathology in PS19 mice *in vivo* [66]. Contribution of EVs to tau pathology
370 development in AD patients has been questioned, however, due to the scarcity of tau in the EV
371 fractions of biofluids. We have witnessed here that EVs containing only 300 pg of tau
372 successfully induced templated misfolding in endogenous tau and subsequently transferred tau
373 pathology through the entire hippocampus in aged B6 mice, indicating that EVs are indeed
374 vehicles to transfer pathological tau. AD-EVs show higher transmissibility of tau via increased
375 uptake by recipient neurons. Our proteome analysis of AD brain-derived EVs suggests
376 enrichment of glia-derived EVs rather than neuron-derived EVs [23]. Interestingly, recent
377 analysis of single cell RNAseq of human AD brains showed that CD81, an established
378 tetraspanin exosomal marker, is highly expressed in the microglia module [67] together with
379 ApoE, the most prominent AD GWAS gene [68]. Notably, APOE is a representative disease-
380 associated / neurodegenerative microglia (DAM/MGnD) genes [69], suggesting active EV and
381 APOE synthesis in DAM/MGnD in AD brains. CD81 and CD82 are known to regulate the
382 integrin cluster distribution on plasma membranes to facilitate dendritic cell adhesions [70] and
383 recruit integrins to endosomal pathway [71] respectively. In addition, our recent study
384 demonstrates that IL-1β-stimulated astrocytes secrete EVs enriched in the integrin family with
385 higher neuronal uptake efficiency, which was inhibited by an integrin-blocking peptide [24].
386 Thus, EV uptake in AD brains could be enhanced by differentially expressed EV surface proteins
387 due to altered cargo sorting or the origin of the cell type in neuroinflammatory conditions.
388 Dysfunction of interneuron has been extensively reported in tauopathy animal models [72, 73].

389 JNPL3 transgenic mice harboring *MAPT* P301L mutation show loss of hippocampal interneurons,
390 PHF1^{+} p-tau and MC1^{+} misfolded tau in interneurons ,and rescue of enhanced later-phase long-
391 term potentiation by administration of $GABA_A$ receptor agonist [72]. VLW mice overexpressing
392 human *MAPT* with 3 mutations (G272V, P301L, and R406W) show p-tau accumulation in
393 hippocampal PV^{+} GABAergic neurons and mossy cells in DG as early as 2 months of age [73].
394 Reduction of GABAergic septohippocampal innervation on PV^{+} interneurons in VLW mice
395 suggests tau accumulation may be responsible for GABAergic neuronal loss [73]. We found that
396 EV-mediated tau propagation is explicitly in GABAergic neurons, including PV neurons
397 followed by mossy cells, and GABAergic dysfunction was determined by both
398 electrophysiological recording and c-fos activity, indicating the susceptibility of those neurons to
399 tau toxicity. PV neurons are surrounded by the specific extracellular matrix (ECM), called
400 perineuronal nets, comprised of integrin-binding versican and heparin sulfate proteoglycan
401 (HSPG) [74]. Since EV uptake is dependent on HSPG [38], EV surface proteins such as integrins,
402 which are known to interact with HSPG, may play a potential role on their uptake by
403 GABAergic neurons.
404 In summary, we have revealed that the mechanism of EV-mediated tau propagation via highly
405 transmissible and potent seeding activity of AD-EVs with selective susceptibility of GABAergic
406 neurons. Our study created a foundation to elucidate the novel EV-mediated tau spread
407 mechanism, which may be relevant to interneuron dysfunction in AD.
408

409 **Materials and Methods**

410 **Animals**

411 Aged C57BL/6 (18-19 months old), Tau KO (B6.129X1-*Mapt*^{tm1Hnd}/J, # 007251) and pregnant
412 CD-1 mice were purchased from National Institute of Aging (NIA), Jackson laboratory and
413 Charles River Laboratory, respectively. B6 mice were used for intracerebral inoculation of
414 human brain-derived materials. Adult Tau KO mice were used for isolation of brain-derived
415 EVs. E16 CD-1 mice were used for primary culture of cortical neurons. All animal procedures
416 followed the guidelines of the National Institutes of Health Guide for the Care and Use of
417 Laboratory Animals, and were approved by the Boston University Institutional Animal Care and
418 Use Committee (IACUC).

419 **Isolation of EVs from AD brains**

420 Human and mouse brain-derived EVs were isolated according to our recently published methods
421 [22]. Briefly, fresh frozen human frontal cortex gray matter was sliced with a razor blade on ice
422 while frozen to generate 1–2 cm long, 2–3 mm wide sections. The cut sections are dissociated
423 while partially frozen in 300 μL of 20 units papain (# LK003178, Worthington Biochemical
424 Corporation) in 15 mL Hibernate-E media (Thermo Fisher Scientific) at 37°C for 15 min, and
425 protease and phosphatase inhibitors (# PI78443, Thermo Fisher Scientific) were added. The
426 tissue sample was centrifuged at 300 × *g* for 10 min at 4°C. The pellet was used as the brain
427 homogenate control. The supernatant was centrifuged at 2000 × *g* for 10 min at 4°C. The
428 supernatant was centrifuged at 10,000 × *g* for 10 min at 4°C. The supernatant was transferred
429 through a 0.22-μm filter and ultracentrifuged at 100,000 × *g* for 70 minutes at 4°C using
430 Beckman SW41Ti. The pellet was resuspended in 2 mL of 0.475M of sucrose in double-filtered
431 PBS with 0.22-μm filter (dfPBS) and overlaid on 5 sucrose cushions (2 mL each of 2.0M, 1.5M,
432 1M, 0.825M, 0.65M in dfPBS) and ultracentrifuged at 100,000 × *g* for 20 h. The samples were
433 fractionated in 1-mL step, and fractions V and VI are collected as EV-enriched fraction. Each

434 fraction was ultracentrifuged at 100,000 × *g* for 70 minutes at 4ºC to pellet EVs, which were
435 resuspended in 30 uL dfPBS as a final volume/fraction.

436 **Nanoparticle Track Analysis (NTA)**

437 The number of EVs in the enriched fraction was analyzed as previously described [22, 75].
438 Briefly, all samples were diluted in dfPBS for at least 1:1000 or more to get particles within the
439 target reading range for the Nanosight 300 machine (Malvern Panalytical Inc), which is 10-100
440 particles per frame. Using a syringe pump infusion system (Harvard Laboratories/Malvern), five
441 60-second videos were taken for each sample at 21°C constant. Analysis of particle counts was
442 carried out in the Nanosight NTA 3.3 software (Malvern Panalytical Inc) with a detection
443 threshold of 5. Particle counts were normalized for dilution on the machine, dilution of the final
444 pellet, and starting material for exosome extraction. The average count was then taken for
445 fractions V and VI.

446 **Atomic force microscopy (AFM)**

447 Ten μL of EVs (~1 μg/μL) were incubated with 100 μL 0.5% sarkolsyl (#61747-100ML, Sigma-
448 Aldrich) for 30 min on ice in ultracentrifuge-compatible Beckman microcentrifuge tubes for
449 solubilization of vesicles, and dfPBS was added to 1.2mL. The sample was ultracentrifuged at
450 100,000 × *g* for 70min at 4°C. The supernatant was removed but leaving 50 μL, and dfPBS was
451 added to 1.2mL for second ultracentrifugation at 100,000 × *g* for 70 min at 4°C. The pellet was
452 dissociated in 10 μL dfPBS, and subjected to AFM imaging by ScanAsyst mode with Multimode
453 8 AFM machine (Bruker, Billerica MA) as previously described [76].

454 **Transmission Electron microscopy (TEM)**

455 TEM of EVs was conducted as previously described [15, 22]. Briefly, 5 μL of the EV sample
456 was adsorbed for 1 min to a carbon-coated grid (# CF400-CU, Electron Microscopy Sciences)

457 that had been made hydrophilic by a 20-sec exposure to a glow discharge (25mA). Excess liquid
458 was removed with a filter paper (#1 Whatman), the grid was then floated briefly on a drop of
459 water (to wash away phosphate or salt), blotted on a filer paper, and then stained with 0.75%
460 uranyl formate (#22451 EMS) for 15 seconds. After removing the excess uranyl formate with a
461 filter paper, the grids were examined in a JEOL 1200EX Transmission electron microscope and
462 images were recorded with an AMT 2k CCD camera.

463 **ELISA of brain tissue extraction and EV samples**

464 Brain tissue homogenate and EV samples were diluted 1:10 in 8M guanidine buffer so
465 solubilization, followed by dilution in TENT buffer (50 mM Tris HCl pH 7.5, 2 mM EDTA,
466 150mM NaCl, 1% Triton X-100) supplemented with phosphatase inhibitors (Pierce HALT
467 inhibitor), and subjected to human total tau ELISA (human tau: # KHB0042, Thermo Fisher
468 Scientific) according to manufacturer's instructions.

469 **EV labelling with PKH26**

470 EVs were labelled with lipophilic red fluorescent dye (PKH26, Sigma-Aldrich), according to the
471 manufacturer's protocol. Briefly, 0.32-μL PKH26 dye was mixed with 10 μL EV samples in 40
472 μL diluent C, and incubated for 5 min at room temperature. dfPBS was used as a negative
473 control. The labelling reaction was stopped by adding 50 μL chilled dfPBS, and subjected to
474 Exosome Spin Columns (MW 3000, ThermoFisher, cat.4484449) at 750 × *g* for 2 min to remove
475 the free dye and enrich the labelled EVs, which was adjusted to 5 μg/100 μL for the neuronal EV
476 uptake assay.

477 **Primary tissue culture of murine cortical neurons**

478 Primary murine cortical neurons were isolated from E16 embryos from pregnant CD-1 mice
479 (Charles River Laboratory). Dissociated cortical tissues were digested with trypsin-EDTA

480 (diluted to 0.125%, #25200072, Invitrogen), triturated by polished pipettes, and strained into
481 single neurons using a 40-μm pore size Falcon cell strainer (Thermo Fisher Scientific), and
482 plated onto 12-mm #1 thickness coverslips or plates, precoated with 100 μg/mL poly-D-lysine
483 (Sigma-Aldrich) diluted in borate buffer (0.05 M boric acid, pH 8.5) and washed with sterile
484 water prior, at 375,000 cells per coverslip in 24-well plates. Neurons at DIV7 were treated with
485 PKH26-labeled EVs for EV uptake or tau transfer study.

486 **Tau seeding assay**

487 HEK-TauRD P301S FRET cells were plated at in 96-well PDL coated plate (# 354461, Corning)
488 in growth media (DMEM, 10%FBS). The day after, human brain-derivied EVs were mixed with
489 80 μL Opti-MEM and 20 μL Lipofectamine 2000, and incubated at room temperature for 10 min.
490 Subsequently, growth media was removed from the cells, replaced with samples containing
491 Lipofectamine, and incubated at 37°C, 5%CO_2. After 1 h, Lipofectamine-containing media was
492 removed from the cells and replaced with growth media. Cells were maintained in culture at
493 37°C, 5% CO_2 for 72 h afterward. The day of the analysis, cells were washed in PBS, detached
494 with Trypsin 0.25% (#25200072, Invitrogen) and washed with FACS buffer (PBS + 0.5% BSA).
495 Subsequently, cells were fixed in 2%PFA, 2% Sucrose for 15 min at 4 °C, spun at 12,000 rpm for
496 15 min at 4 °C, resuspended in FACS buffer and acquired with a 5 lasers system LSRII (Becton
497 Dickinson), using pacific-orange and pacific-blue dyes for YFP and CFP, respectively. Data was
498 analyzed by FlowJo and expressed as Integrated FRET Density.

499 **Stereotaxic surgery**

500 B6 mice at 18–19 months old were deeply anesthetized with isoflurane and immobilized in a
501 stereotaxic frame (David Kopf Instruments) installed with robot stereotaxic injection system
502 (Neurostar). Animals were unilaterally inoculated with human brain-derived EVs or tau

503 aggreagtes in the dorsal hippocampal OML (bregma: −2.18 mm; lateral: 1.13 mm; depth: −1.9
504 mm from the skull) using a 10-μL Hamilton syringe as previously described [15]. Each injection
505 site received 1.0 μL of inoculum, containing 300 pg tau /μL. We noted that majority of the
506 injected materials were deposited at the OML of the hippocampus (Fig. 3A).

507 **Immunochemistry and Immunofluorescence**

508 Brains were removed after transcardial perfusion fixation with ice-cold 4%
509 paraformaldehyde/PBS followed by post-fixation for 16h and cryoprotection with 15% then 30%
510 sucrose/PBS over 3-5 days. They were cut coronally in 20-μm thickness using a cryostat, and
511 three hippocampal sections separated at least 200 μm per mouse per antibody were used for IHC.
512 The sections were processed by antigen retrieval with Tris-EDTA (pH 8.0) at 80°C,
513 permeabilized in 0.5% Triton-X 100/PBS, and blocked in 10% normal goat serum, 1% BSA, and
514 0.1% tween-20 in PBS. Sections were incubated GAD67 (#PA5-36054, ThermoFisher
515 scientific); GAD67-biotin-conjugated (# MAB5406B, Millipore), AT8 (# MN1020,
516 ThermoFisher scientific), GluR2/3 (# AB1506, Millipore), MAP-2 (# PA517646, Invitrogen), c-
517 fos (# 226 003, Synaptic Systems), PS422 (# 44-764G, ThermoFisher scientific), Alz50 and
518 MC1, CP13, PHF-1 (as kind gifts provided by Dr. Davis Peter), diluted with 1% BSA, 0.025%
519 tween-20 in PBS at 4°C for overnight (see Supplementary Table S3 for antibody information).
520 Sections were then washed and incubated in secondary antibodies (AlexaFluor 594 goat anti-
521 mouse; 1:1000, AlexaFluor488 goat anti-rabbit; 1:1000, AlexaFluor568 streptavidin 1:1000) for
522 1 h at room temperature. All images were captured on Nikon deconvolution wide-field
523 epifluorescence system (Nikon Instruments) or confocal microscopic imaging as described below.

524 **Confocal image processing and quantification by Imaris**

525 All confocal imaging was performed on a LSM710 using Zen 2010 software (Zeiss) or a Leica
526 TCS SP8 lightning microscope at the inverted Leica DMi8 microscope stand using the confocal
527 mode with a 63× oil immersion/1.4 N.A objective using a 1.1 optical zoom at a pinhole of 1.0
528 Airy units. Images of 2048 × 2048 pixels as confocal stacks with a z-interval of 0.35 μm was
529 used to image cells. For imaging GAD67 puncta, a 555-nm laser line was used and emission was
530 collected at 565–650 nm. Gain and off-set were set at values which prevented saturated and
531 empty pixels. After image acquisition, all images were applied with lightning deconvolution.
532 The quantification of GAD67 positive puncta was counted by using the "spot" module of Imaris
533 9.5, 64-bit version (Bitplane AG, Saint Paul, MN, www.bitplane.com). Manual cutting of the
534 CA1 pyramidal cells with GAD67 fields in 3D. This program analyzes stacks of confocal
535 sections acquired in two channels (red for GAD67, blue for DAPI represents cell number). Final
536 data analysis was performed using Microsoft Excel and Graph rendering was done in GraphPad
537 Prism

538 **Biochemical sequential extraction from mouse brains**

539 Brain tissues were removed from CTRL-EV, pAD-EV and AD-EV-injected mice at the
540 designated time points after transcardial perfusion of animals by ice-cold PBS to minimize
541 contamination of blood-derived mouse immunoglobulins. Hippocampal and cortical regions
542 were dissected separately, snap frozen in dry ice and stored at −80 °C before protein extraction.
543 For enrichment of tau oligomers and fibrils, sequential extractions were performed as follows:
544 Each hippocampal tissue was homogenized in 9 volumes of TBS buffer (50 mM Tris-Cl, pH 8.0
545 in saline) supplemented with protease and phosphatase inhibitor cocktails (# PI78443, Thermo
546 Fisher Scientific). The homogenate was centrifuged at 48,300 × *g* for 20 min at 4 °C. The
547 supernatant and pellet is designated as S1 (TBS-supernatant) and P1 (TBS-pellet) fraction,

548 respectively. The S1 fraction was ultracentrifuged at 186,340 × *g* at 4 °C for 40 min. The pellet
549 fraction (S1p) was resuspended in a 4 volume of double-filtered TE buffer relative to the starting
550 weight of the tissue, aliquoted and frozen at -80°C as tau oligomer-enriched fraction. The P1
551 fraction was resuspended in 5 volume of wet weight of the original tissue of buffer B (1%
552 sarkosyl, 10 mM Tris, pH 7.4, 800 mM NaCl, 10% sucrose, 1 mM EGTA, 1 mM PMSF, all from
553 Sigma-Aldrich) and incubated by rotating with the bench top thermomixer at 37 °C for 1 h. The
554 sample was ultracentrifuged at 186,340 × *g* for 1 h at 4 °C. After completely removing the
555 supernatant and rinsing the pellet in sterile PBS, sarkosyl-insoluble pellet (P3) was resuspended
556 with 50 μL double-filtered TE buffer (10 mM Tris, 1 mM EDTA, pH 8.0), aliquoted and frozen
557 at -80°C as tau fibril-enriched fraction.

558 **Western and dot blotting**

559 For western blotting, homogenates (Ho) of hippocampus from each experimental group and an
560 equal proportion of corresponding Ho, S1, S1p and P3, were loaded on 10% SDS–PAGE gels (
561 Bio-Rad) and electro-transferred to 0.45-μm nitrocellulose membranes (Bio-Rad). For dot
562 blotting, an equal volume of EVs sample were dotted onto 0.45-μm nitrocellulose membranes
563 (Bio-Rad) and washed twice with TBS buffer. The nitrocellulose membranes were then blocked
564 in freshly prepared 5% skim milk diluted in TBS before being immunoblotted with specific
565 primary antibodies (Supplementary Table 3). The membrane were further incubated with HRP-
566 labeled secondary antibodies and scanned using C300 digital chemiluminescent imager (Azure
567 Biosystems). The optical densities were measured using Image J software. The full-length gels
568 for the cropped blots shown in the main figures are presented in Supplementary Figure 5.

569 **Whole cell patch clamp recording**

570 ***Preparation of Brain Slices for Recording and Filling***

571 Immediately after decapitation, mouse brains were rapidly removed and placed in oxygenated
572 (95% O_2 and 5% CO_2) ice-cold Ringer's solution containing following ingredients (in mM): 25
573 $NaHCO_3$, 124 NaCl, 1 KCl, 2 KH_2PO_4, 10 glucose, 2.5 $CaCl_2$, 1.3 $MgCl_2$ (pH 7.4; Sigma-
574 Aldrich). A total of four to five 300-µm thick acute coronal sections containing the hippocampus
575 were obtained from each subject. Over an 8-10 h period, slices were individually transferred
576 from the incubation chamber to submersion-type recording chambers (Harvard Apparatus,
577 Holliston, MA) affixed to the stages of Nikon E600 infrared-differential interference contrast
578 (IR-DIC) microscopes (Micro Video Instruments, Avon, MA) with a water-immersion lens (40×,
579 0.9 NA; Olympus) for recording. During recordings, slices were superfused in room-temperature
580 Ringer's solution bubbled with carbogen (95% O_2, 5% CO_2) a rate of 2.5 ml/min. Whole-cell
581 patch clamp recordings were obtained from the soma of visually identified CA1 pyramidal cells
582 in both the dorsal and ventral hippocampus of ipsilateral side of the brain. Electrodes were
583 created from borosilicate glass with a Flaming and Brown micropipette puller (Model P-87,
584 Sutter Instruments). These pulled patch pipettes were filled with potassium methanesulfonate
585 (KMS) based intracellular solution, with concentrations in mM as follows: (KCH_3SO_3 122,
586 $MgCl_2$ 2, EGTA 5, Na-HEPES 10, Na_2ATP 5)., and had a resistance of 5.5–6.5 MΩ in external
587 Ringer's solution.

588 ***Physiological Inclusion Criteria***

589 Single AP properties (including threshold, amplitude, Action potential Half-Width (APHW), rise
590 and fall) were measured on the second evoked AP in a 200 ms current-clamp series that
591 preferentially evoked 3 or more action potentials after depolarizing step-current. We proceeded
592 to High Rn or Low Rn only if neurons were unable to elicit AP at 200 ms. AP half-width was
593 computed at half-max of AP amplitude, where the amplitude was measured from the threshold to

594 the absolute peak of the spike. All the quantification for AP properties was carried out in an
595 expanded timescale, and the linear measure tool we used in FitMaster analysis software (HEKA
596 Elektronik) to measure all single AP properties. An algorithm designed in Matlab was used to
597 automatically detect these parameters. In the few cases where it failed to do so, a manual
598 detection method was used. The final paradigm in the Current-clamp configuration was to inject
599 2 s hyperpolarizing and depolarizing steps (-100 to +120 pA with increments of 20 pA or -220
600 pA to +330 pA with increments of 50pA, 12.5kHz sampling frequency) in order to assess
601 repetitive AP firing. Those neurons which did not fire repetitively in depolarizing step were
602 discarded. Firing rates in response to current steps were analyzed fitting with a generalized linear
603 model, using the genotype, CA1 pyramidal cells types, rheobase, input resistance, injected
604 current level and their respective interactions as independent variables. Whole-cell voltage clamp
605 was used to measure AMPA receptor-mediated spontaneous excitatory currents (sEPSCs)
606 response for 2 min at a holding potential of -80 mV (6.67 kHz sampling frequency). The same
607 neuron was held at -40 mV (6.67 kHz sampling frequency) for 2 minutes in order to obtain
608 enough sample size to measure GABA receptor-mediated spontaneous inhibitory currents
609 (sIPSCs). All recorded traces were run through Minianalysis software (Synaptosoft) which
610 allowed for quantification of synaptic current properties such as frequency, amplitude, area, time
611 to rise and time to decay. To determine the kinetics of EPSCs and IPSCs, the rise and decay of
612 averaged traces were each fit to a single-exponential function. In all of the synaptic current
613 measurements, the event detection threshold was set at the maximum root mean squared noise
614 level (5 pA). All neurons had resting membrane potentials between −55 and −75 mV (somatic
615 recordings) and were confirmed to have intact somas and apical tufts.

616 **Statistical Analyses**

All data are presented as means ± standard error of the mean (s.e.m). Comparisons between two groups were done by two-tailed paired or unpaired Student's *t*-tests. Multiple comparisons were performed by either one- or two-way ANOVA, followed by Bonferroni's or Dunnett's *post hoc*. Statistical analyses were performed using Prism 8.0 (GraphPad Software). A statistically significant difference was assumed at $p < 0.05$.

Acknowledgement: We would like to thank J-C Delpech, Annina M. DeLeo, and other members of the Laboratory of Molecular NeuroTherapeutics for scientific suggestions and technical assistance, and Dr. Peter Davies for the generous gift of the Alz50, MC1, CP13 and PHF1 monoclonal antibodies.

Funding: This work was funded in part by NIH R01AG066429 (TI), RF1AG054199 (TI), NIH R01AG054672 (TI), NIH R56AG057469 (TI), NIH R21NS104609 (TI), Alzheimer's Association AARF-9550302678 (SM), Cure Alzheimer's Fund (TI), BrightFocus Foundation (A2016551S), CurePSP (TI) and BU ADC NIH P30AG0138423 (ZR, SI).

Author contributions: Conceptualization, Z.R., A.M.D., S.I., J.L. and T.I.; Methodology, Z.R., D.P., A.Y-K., S.M., S-V.K., K.T-K., S.G., R.K., H.E.G., Y.W., J.L.; Bioinformatics: J.H.; Image analysis, Z.R, J.H, A.Y-K., S-V.K., YW; Manuscript writing & Editing, Z.R., D.P., T.I., S.I.; All authors read and approved the final manuscript.

Conflict of Interest:

The authors declare no conflict of interest in this manuscript

640

641 **Figure legends**

642 **Figure 1. Characterization of EVs using dot blot with TEM, nanoparticle tracking analysis,**

643 **tau oligomer dot-blotting and atomic force microscopy**

644 **A.** Schematic of EV separation from human frozen brain tissue.

645 **B.** TEM image of human brain-derived EVs.

646 **C-E.** Nanoparticles tracking analysis (NTA) of isolated EVs (C), quantification of EV density

647 (D) and EV size (E).

648 **F-K**. Semi-quantification of tau oligomers in EVs by multiple tau oligomer antibodies. Dot blot

649 images shown in Supplementary Fig. 1. $^{*}p < 0.05$, $^{**}p < 0.01$, as determined by one-way

650 ANOVA (alpha = 0.05) and Dunnett's *post-hoc*. Graphs indicate mean ± s.e.m. Each dot

651 represent individual subject, 3 replicates per subject, 3 donors per group, .

652 **L-M.** Atomic force microscopy (AFM) images showing brain-derived EV-tau oligomers isolated

653 from CTRL, pAD, and AD brains (L). Size distribution histogram of EV-tau oligomers (M). $^{*}p$

654 < 0.05 and $^{****}p < 0.0001$ for pAD-EVs vs. CTRL-EVs; $^{\#\#}p < 0.01$, and $^{\#\#\#\#}p < 0.0001$ for AD-

655 EVs vs. CTRL-EVs as determined by one-way ANOVA (alpha = 0.05) and Dunnett's *post-hoc*.

656 Graphs indicate mean ± s.e.m. n=3 images per sample, 2 samples per group.

657

658 **Figure 2. Neuronal uptake, tau transfer efficiency and tau seeding activities of human**

659 **brain-derived EVs**

660 **A.** A diagram illustrating the primary culture model with primary neuronal or biosensor cells

661 employed to measure the transfer of the brain derived EVs containing Tau.

662 **B.** Cellular uptake of PKH26-labeled EVs (red) by primary culture murine cortical neurons
663 (MAP-2, green; DAPI, blue). Original magnification: 20× (left and middle columns); 40× (right
664 column, taken by Zeiss LSM710 confocal microscopy). Scale bars = 40, 20, 10 μm (left to right).
665 **C.** Quantification of PKH26 fluorescent intensity in MAP-2^+ neurons. $^{****}p < 0.0001$ compared
666 with PBS or Dye only group; $^{\#\#}p < 0.01$ compared with CTRL-EV group; *n.s* denotes no
667 significance as determined by one-way ANOVA (alpha = 0.05) and Dunnett's *post-hoc*. Each dot
668 represents average data per cell in one image (10-20 cells per image), 30 images per group (for
669 PBS and dye ony), 10 images per donor and three donors per group (for CTRL-EV, pAD-EV and
670 AD-EVs), total N = 30 per group.
671 **D.** Total human tau ELISA of neuronal cell lysates. $^{*}p < 0.01$ compared with pAD-EV group; $^{\#\#}p$
672 < 0.01 compared with CTRL-EV group; as determined by one-way ANOVA (alpha = 0.05) and
673 Dunnett's *post-hoc*. Three donors per group, three independent experiments. Graphs indicate
674 mean ± s.e.m.
675 **E.** EVs were tested in the Tau-FRET assay for Tau seeding activity. Results are plotted as
676 Integrated FRET Density values for each sample. $^{\#\#\#}p < 0.001$ compared with CTRL-EV group;
677 as determined by one-way ANOVA (alpha = 0.05) and Dunnett's *post-hoc*. Three donors per
678 group, and each dot represents one well. Graphs indicate mean ± s.e.m. **B-E**: Three donors per
679 group, and the data is representative of three independent experiments.
680
681 **Figure 3. AD-EV and pAD-EV but not CTRL-EV injection causes progressive tauopathy in**
682 **aged B6 mouse brains.**
683 **A**. A scheme illustrating 300 pg of tau containing EVs from human brain unilaterally injected to
684 the hippocampus of B6 mice at 18-19 months of age. DiI (red) indicated the injection site of

685 outer molecular layer of hippocampus.

686 **B.** Representative image of AT8 staining (red) 4.5 months after intrahippocampal injection of

687 AD-EV into aged B6 mouse brain. Scale bar = 200 μm (left), 50 μm (right).

688 **C**. Semiquantitative analysis of AD-like tau pathologies based on AT8 immunostaining of brains

689 from CTRL-EV, pAD-EV and AD-EV-injected mice at 4.5 months post injection.

690 **D.** Quantification of AT8 immunostained area in hippocampal region. $^{*}p < 0.05$ and $^{**}p < 0.01$

691 compared with CTRL-EV group; *n.s* denotes no significance as determined by one-way ANOVA

692 (alpha = 0.05) and Dunnett's *post-hoc*. Total mice in each group for the quantification are 4, 6,

693 12, 12, 11 for saline, Tau-KO, CTRL, pAD and AD. Two donors for EVs per group for CTRL,

694 pAD and AD (n = 5-6 mice per donor). At least two sections were imaged per mouse. Each dot

695 represents mean value from one animal. Graphs indicate mean ± s.e.m. **E.** Immunoblotting of

696 biochemically fractionated brain tissue samples for homogenate (Ho), TBS supernatant (S1), tau

697 oligomer enriched (S1p) and tau fibril enriched fractions (P3) by Tau-5 (total tau) and PHF1

698 (pSer396/pSer404 tau) (top panels) and their quantification (bottom panels). Equal proportions of

699 Ho, S1, Sp1 and P3 fractions were analyzed. Three pairs of mice were quantified. Optical density

700 (OD) was normalized to that for the homogenate fraction from each corresponding mouse. $^{*}p <$

701 0.05 and $^{**}p < 0.01$ compared with CTRL group as determined by one-way ANOVA (alpha =

702 0.05) and Dunnett's *post-hoc*. Graphs indicate mean ± s.e.m.

703

704 **Figure 4. EV-tau but not oligomeric or fibril tau enriched samples derived from the same**

705 **AD brain induced tau propagation in mouse brain**

706 **A**. Representative images of PHF1 immunoblotting of isolated EVs, tau oligos and tau fibrils by

707 PHF1 antibodies.

708 **B**. AFM images of EVs and tau aggregates isolated from the same AD brain tissues.

709 **C.** Representative images of AT8 immunostained recipient mice after unilateral injection of AD-
710 EVs (left), tau oligomer-enriched fraction (middle) and tau fibril-enriched fraction (right) in
711 cortical region (top panels) and dentate gyrus (bottom panels).

712 **D.** Quantification of $AT8^+$ neurons in the hippocampus of recipient mice. $^{****}p < 0.0001$
713 compared between EV-tau injected group and oligomeric or fibril tau group, as determined by
714 one-way ANOVA (alpha = 0.05) and Turkey's post-hoc. EV-tau, oligomeric and fibril tau group:
715 n = 4-6 mice per group for quantification. At least two sections were imaged per animal. Each
716 dot represents mean value per animal. Graphs indicate mean ± s.e.m.

717

718 **Figure 5. Co-localization of pathological tau staining with AT8 antibody in GABAergic**
719 **interneurons in the hippocampus of B6 mice**

720 **A**. AT8 (red) and GAD67 (green) immunostaining in the ipsilateral dental gyrus of hippocampal
721 region from CTRL-EV, pAD-EV and AD-EV-injected mice at 4.5 months post injection.

722 **B.** AT8 (red) and GAD67 (green) immunostaining in the ipsilateral CA1 and CA3 of
723 hippocampal region from AD-EV-injected mice.

724 **C-E.** Quantification of $GAD67^+$ cells in DG (C), CA1 (D) and CA3 of hippocampus (E). The
725 percentage of $AT8^+$ $GAD67^+$ cells in all GAD67 positive cells are shown in the right column (C-
726 E). $^{*}p < 0.05$ and $^{**}p < 0.01$ compared with CTRL group, as determined by one-way ANOVA
727 (alpha = 0.05) and Dunnett's *post-hoc*. n = 5-6 mice per group for quantification. At least two
728 sections were imaged per animal. Each dot represents mean value per animal. Graphs indicate
729 mean ± s.e.m.

730 **F-G.** Immunostaining of GluR2/3$^+$ mossy cells (F) and AT8 in the ipsilateral dental gyrus of
731 hippocampal region from AD-EV injected mice; and quantification of the ratio of GAD67$^+$AT8$^+$
732 cells / total AT8$^+$cells (blue) and GluR2/3$^+$ AT8$^+$ cells / AT8$^+$ cells (red). n = 6 mice per group
733 for quantification. At least two sections were imaged per animal. Each dot represents mean value
734 per animal. Graphs indicate mean ± s.e.m.
735
736 **Figure 6. Reduction in GAD67$^+$ puncta around CA1 pyramidal cells and c-fos expression in**
737 **GAD67$^+$ GABAergic neurons in pAD-EV or AD-EV-injected aged B6 mice**
738 **A.** High-magnification images in top panels compared GAD67 expression (red) in CA1
739 pyramidal cells of hippocampus all four injected Tau-KO-, CTRL-, pAD- or AD-EV groups .
740 Second panel are lower-magnification images of GAD67 expression and DAPI staining. Third
741 panel was cell counted by Imaris software based on DAPI staining. Fourth panel was GAD67+
742 puncta analysis by Imaris. Scale bar: 10 μm.
743 **B-C.** Quantification of GAD67$^+$ puncta (B) and total cell number in CA1 of hippocampus (C). $^*p$
744 < 0.05 and $^{**}p < 0.01$ pAD compared with Tau-KO and CTRL-EV group, as determined by one-
745 way ANOVA (alpha = 0.05) and Dunnett's *post-hoc*. n = 4-6 mice per group for quantification.
746 At least two sections were imaged per animal. Each dot represents mean value per animal.
747 Graphs indicate mean ± s.e.m.
748 **D-E.** GAD67 (red) and c-fos (green) co-staining images (D) and quantification of the percentage
749 of c-fos$^+$ GAD67$^+$ cells in all GAD67 positive cells (E) in CA1 region. Scale bar: 10 μm. $^*p <$
750 0.05 and $^{**}p < 0.01$ pAD compared with Tau-KO and CTRL-EV group, as determined by one-
751 way ANOVA (alpha = 0.05) and Dunnett's *post-hoc*. n = 4 mice per group for quantification. At

752 least two sections were imaged per animal. Each dot represents mean value per animal. Graphs
753 indicate mean ± s.e.m.
754 **F-G.** GAD67 (red) and c-fos (green) co-staining images (F) and quantification of the percentage
755 of c-fos^{+} GAD67^{+} cells in all GAD67 positive cells (G) in DG region. Scale bar: 100 μm. $^{*}p <$
756 0.05 and $^{**}p < 0.01$ pAD compared with Tau-KO and CTRL-EV group, as determined by one-
757 way ANOVA (alpha = 0.05) and Dunnett's *post-hoc*. n = 4 mice per group for quantification. At
758 least two sections were imaged per animal. Each dot represents mean value per animal. Graphs
759 indicate mean ± s.e.m.
760
761 **Figure 7. whole-cell current clamp recording of CA1 pyramidal neurons**
762 **A**. Confocal z stack montage (63× magnification) image of biocytin-filled mouse CA1 pyramidal
763 neurons after recording.
764 **B-G**: Action potential (AP)-firing recorded in whole-cell current clamp mode; **B**: Representative
765 traces for Tau KO (black color), pAD (blue color), and AD-EV (red color) for 100 pA step at 2 s
766 long High Rn protocol. **C**. Quantification of repetitive firing at High-Rn step current injection
767 protocol. $^{**}p<0.01$ vs. Tau KO-EV group as determined by RM-ANOVA; **D**: pAD-EV
768 significantly reduce the firing at 100 pA; **E**: Quantification of repetitive firing at Low-Rn step
769 current injection protocol. $^{*}p<0.05$ vs. Tau KO-EV group as determined by RM-ANOVA; **F**:
770 pAD-EV significantly reduced the firing rate at and + 130 pA of step current; **G**. AD-EV
771 significantly reduced AP amplitude. **C-G**: n = 30, 50, and 57 cells for Tau KO, pAD and AD-
772 injected mice, 5-7 mice per group. Each dot represents one recorded cell. Graphs indicate mean ±
773 s.e.m.

774 **H-I**: Quantification of GABAergic spontaneous inhibitory postsynaptic currents (sIPSCs)
775 recorded in neuronal network. pAD showed significant decrease in sIPSC amplitude (H) and E-I
776 amplitude ratio (I). $^{*}p < 0.05$ compared with CTRL group, as determined by one-way ANOVA
777 (alpha = 0.05) and Dunnett's *post-hoc*. H-I: n = 18, 23, and 28 cells for Tau KO, pAD and AD-
778 injected mice, 5-7 mice per group. Each dot represents one recorded cell. Graphs indicate mean ±
779 s.e.m. See also Supplementary Tables S4-S7.
780
781 **Supplementary Figure S1. Dot blot of Tau KO and human brain-derived EV samples by**
782 **tau oligomer-specific antibodies.**
783
784 **Supplementary Figure S2. AT8 staining of young and aged mice after injected of human**
785 **brain-derived EVs.** Young (2 months old) or Aged (18 months old) mice were stereotaxically
786 injected with human brain-derived EVs (CTRL, pAD or AD) containing 300 pg tau in 1 μL
787 volume into the outer molecular layer of dentate gyrus, and sacrificed 4.5 months after the
788 injection for the neuropathological examination using AT8 (pSer202/pSer205 tau) monoclonal
789 (red) and counterstained with Dapi (blue). Coronal sections depicting the ipsilateral hippocampal
790 region (left) and hilus region (right). Sale bars: 200 μm (left) and 50 μm (right)
791
792 **Supplementary Figure S3. Tau pathology staining with Alz50, MC1, CP13, PS422 and**
793 **PHF1 antibodies.** Representative images of AT8 (pSer202/pSer205 tau, A), Alz50
794 (conformation-specific misfolded tau, B), MC1 (conformation-specific misfolded tau, C), CP13
795 (pSer202 tau, D), PS422 (pSer422 tau, E) and PHF1 staining (pSer396/pSer404 tau, F) (red) and
796 Dapi (blue) 4.5 months after intrahippocampal injection of saline, Tau KO-EV, CTRL-EV, and

797 pAD-EV or AD-EV (1 μL volume containing 300 pg tau) into aged B6 mouse brain. Scale bar =
798 200 (left) and 100μm (right).
799
800 **Supplementary Figure S4. Tau accumulation in the injection site of cortex 4.5 months post**
801 **intracranial injection.** Aged mice (18 months of age) were intracranially injected with AD-EV
802 (left), tau oligomer-enriched fraction (middle) or tau fibril-enriched fraction (right) containing
803 300 pg tau in 1 μL volume. The animals were sacrificed and tested for neuropathology using
804 AT8 (red) and counterstained by Dapi (blue) for nuclear staining. Perikaryal accumulation of p-
805 tau in AD-EV-injected cortical region (left) and neuropil staining in tau oligomer (middle) or
806 fibril-injected cortical region (right). Scale bar: 50 μm.
807
808 **Supplementary Figure S5. AT8$^+$ cell were co-stained with parvalbumin$^+$ inhibitory but not**
809 **neurogranin$^+$ excitatory neurons in the hippocampal region after AD-EV injection.**
810 **A**. AT8 (pSer202/pSer205 tau, red) and parvalbumin (inhibitory neuronal marker, green)
811 immunostaining in the ipsilateral CA1, CA3 and DG regions of hippocampus from AD-EV-
812 injected mice at 4.5 months post injection. Nuclei were conterstained by Dapi (blue). Scale bar:
813 50 μm.
814 **B.** AT8 (red) and neurogranin (excitatory neuronal marker, green) immunostaining of the same
815 brains. Nuclei were conterstained by Dapi (blue). Scale bar: 50 μm.
816
817 **Supplementary Table S1. Demographics of human cases used in the study**
818

819 **Supplementary Table S2. Biochemical characterization of EV-enriched fractions derived**
820 **from human brain**
821
822 **Supplementary Table S3. List of antibodies used in the study**
823
824 **Supplementary Table S4-S8. Electrophysiological properties of CA1 pyramidal cells in**
825 **brain-derived EV-injected mouse brain**
826
827 **References**

828 [1] P.V. Arriagada, J.H. Growdon, E.T. Hedley-Whyte, B.T. Hyman, Neurofibrillary tangles but
829 not senile plaques parallel duration and severity of Alzheimer's disease, Neurology 42(3 Pt 1)
830 (1992) 631-9.
831 [2] H. Braak, E. Braak, Neuropathological stageing of Alzheimer-related changes, Acta
832 Neuropathol 82(4) (1991) 239-59.
833 [3] C.A. Brunello, M. Merezhko, R.L. Uronen, H.J. Huttunen, Mechanisms of secretion and
834 spreading of pathological tau protein, Cell Mol Life Sci (2019).
835 [4] H. Arai, M. Terajima, M. Miura, S. Higuchi, T. Muramatsu, N. Machida, H. Seiki, S. Takase,
836 C.M. Clark, V.M. Lee, et al., Tau in cerebrospinal fluid: a potential diagnostic marker in
837 Alzheimer's disease, Ann Neurol 38(4) (1995) 649-52.
838 [5] H. Zetterberg, D. Wilson, U. Andreasson, L. Minthon, K. Blennow, J. Randall, O. Hansson,
839 Plasma tau levels in Alzheimer's disease, Alzheimers Res Ther 5(2) (2013) 9.
840 [6] S. Saman, W. Kim, M. Raya, Y. Visnick, S. Miro, S. Saman, B. Jackson, A.C. McKee, V.E.
841 Alvarez, N.C. Lee, G.F. Hall, Exosome-associated tau is secreted in tauopathy models and is

842 selectively phosphorylated in cerebrospinal fluid in early Alzheimer disease, J Biol Chem 287(6)
843 (2012) 3842-9.
844 [7] M.S. Fiandaca, D. Kapogiannis, M. Mapstone, A. Boxer, E. Eitan, J.B. Schwartz, E.L. Abner,
845 R.C. Petersen, H.J. Federoff, B.L. Miller, E.J. Goetzl, Identification of preclinical Alzheimer's
846 disease by a profile of pathogenic proteins in neurally derived blood exosomes: A case-control
847 study, Alzheimers Dement 11(6) (2015) 600-7 e1.
848 [8] C.N. Winston, E.J. Goetzl, J.C. Akers, B.S. Carter, E.M. Rockenstein, D. Galasko, E.
849 Masliah, R.A. Rissman, Prediction of conversion from mild cognitive impairment to dementia
850 with neuronally derived blood exosome protein profile, Alzheimers Dement (Amst) 3 (2016) 63-
851 72.
852 [9] J.L. Guo, S. Narasimhan, L. Changolkar, Z. He, A. Stieber, B. Zhang, R.J. Gathagan, M. Iba,
853 J.D. McBride, J.Q. Trojanowski, V.M. Lee, Unique pathological tau conformers from
854 Alzheimer's brains transmit tau pathology in nontransgenic mice, J Exp Med 213(12) (2016)
855 2635-2654.
856 [10] S. Narasimhan, J.L. Guo, L. Changolkar, A. Stieber, J.D. McBride, L.V. Silva, Z. He, B.
857 Zhang, R.J. Gathagan, J.Q. Trojanowski, V.M.Y. Lee, Pathological Tau Strains from Human
858 Brains Recapitulate the Diversity of Tauopathies in Nontransgenic Mouse Brain, J Neurosci
859 37(47) (2017) 11406-11423.
860 [11] J.C. Polanco, B.J. Scicluna, A.F. Hill, J. Gotz, Extracellular vesicles isolated from brains of
861 rTg4510 mice seed tau aggregation in a threshold-dependent manner, J Biol Chem (2016).
862 [12] S. Baker, J.C. Polanco, J. Gotz, Extracellular Vesicles Containing P301L Mutant Tau
863 Accelerate Pathological Tau Phosphorylation and Oligomer Formation but Do Not Seed Mature
864 Neurofibrillary Tangles in ALZ17 Mice, J Alzheimers Dis 54(3) (2016) 1207-1217.

865 [13] C.N. Winston, B. Aulston, E.M. Rockenstein, A. Adame, O. Prikhodko, K.N. Dave, P.
866 Mishra, R.A. Rissman, S.H. Yuan, Neuronal Exosome-Derived Human Tau is Toxic to Recipient
867 Mouse Neurons in vivo, J Alzheimers Dis 67(2) (2019) 541-553.
868 [14] T. Bilousova, C. Elias, E. Miyoshi, M.P. Alam, C. Zhu, J. Campagna, K. Vadivel, B.
869 Jagodzinska, K.H. Gylys, V. John, Suppression of tau propagation using an inhibitor that targets
870 the DK-switch of nSMase2, Biochem Biophys Res Commun 499(4) (2018) 751-757.
871 [15] H. Asai, S. Ikezu, S. Tsunoda, M. Medalla, J. Luebke, T. Haydar, B. Wolozin, O. Butovsky,
872 S. Kugler, T. Ikezu, Depletion of microglia and inhibition of exosome synthesis halt tau
873 propagation, Nat Neurosci 18(11) (2015) 1584-93.
874 [16] Z. Ruan, T. Ikezu, Tau Secretion, Adv Exp Med Biol 1184 (2019) 123-134.
875 [17] M. Colin, S. Dujardin, S. Schraen-Maschke, G. Meno-Tetang, C. Duyckaerts, J.P. Courade,
876 L. Buee, From the prion-like propagation hypothesis to therapeutic strategies of anti-tau
877 immunotherapy, Acta Neuropathol 139(1) (2020) 3-25.
878 [18] H. Mirbaha, B.B. Holmes, D.W. Sanders, J. Bieschke, M.I. Diamond, Tau Trimers Are the
879 Minimal Propagation Unit Spontaneously Internalized to Seed Intracellular Aggregation, J Biol
880 Chem 290(24) (2015) 14893-903.
881 [19] W. Hu, X. Zhang, Y.C. Tung, S. Xie, F. Liu, K. Iqbal, Hyperphosphorylation determines
882 both the spread and the morphology of tau pathology, Alzheimers Dement 12(10) (2016) 1066-
883 1077.
884 [20] L.D. Evans, T. Wassmer, G. Fraser, J. Smith, M. Perkinton, A. Billinton, F.J. Livesey,
885 Extracellular Monomeric and Aggregated Tau Efficiently Enter Human Neurons through
886 Overlapping but Distinct Pathways, Cell reports 22(13) (2018) 3612-3624.

887 [21] G. van Niel, G. D'Angelo, G. Raposo, Shedding light on the cell biology of extracellular
888 vesicles, Nature reviews. Molecular cell biology 19(4) (2018) 213-228.
889 [22] S. Muraoka, W. Lin, M. Chen, S.W. Hersh, A. Emili, W. Xia, T. Ikezu, Assessment of
890 separation methods for extracellular vesicles from human and mouse brain tissues and human
891 cerebrospinal fluids, Methods (2020).
892 [23] S. Muraoka, A. DeLeo, M. Sethi, Y. Yukawa-Takamatsu, Z. Yang, J. Ko, J. Hogan, Z.
893 Ruan, Y. You, Y. Wang, M. Medalla, S. Ikezu, W. Xia, S. Golantra, H. Gendelman, D. Issadore,
894 J. Zaia, T. Ikezu, Proteomic Profiling and Biological Characterization of Extracellular Vesicles
895 Isolated from Alzheimer's Disease Brain Tissues, Alzheimers Dement in press (2020).
896 [24] Y. You, K. Borgmann, V.V. Edara, S. Stacy, A. Ghorpade, T. Ikezu, Activated human
897 astrocyte-derived extracellular vesicles modulate neuronal uptake, differentiation and firing, J
898 Extracell Vesicles 9(1) (2020) 1706801.
899 [25] Y. You, T. Ikezu, Emerging roles of extracellular vesicles in neurodegenerative disorders,
900 Neurobiol Dis 130 (2019) 104512.
901 [26] J.C. Delpech, S. Herron, M.B. Botros, T. Ikezu, Neuroimmune Crosstalk through
902 Extracellular Vesicles in Health and Disease, Trends Neurosci 42(5) (2019) 361-372.
903 [27] A.M. DeLeo, T. Ikezu, Extracellular Vesicle Biology in Alzheimer's Disease and Related
904 Tauopathy, J Neuroimmune Pharmacol 13(3) (2018) 292-308.
905 [28] L.I. Grad, S.M. Fernando, N.R. Cashman, From molecule to molecule and cell to cell:
906 prion-like mechanisms in amyotrophic lateral sclerosis, Neurobiol Dis 77 (2015) 257-65.
907 [29] K.M. Danzer, L.R. Kranich, W.P. Ruf, O. Cagsal-Getkin, A.R. Winslow, L. Zhu, C.R.
908 Vanderburg, P.J. McLean, Exosomal cell-to-cell transmission of alpha synuclein oligomers, Mol
909 Neurodegener 7 (2012) 42.

910 [30] B. Fevrier, D. Vilette, F. Archer, D. Loew, W. Faigle, M. Vidal, H. Laude, G. Raposo, Cells
911 release prions in association with exosomes, Proc Natl Acad Sci U S A 101(26) (2004) 9683-8.
912 [31] S. Dujardin, S. Bégard, R. Caillierez, C. Lachaud, L. Delattre, S. Carrier, A. Loyens, M.C.
913 Galas, L. Bousset, R. Melki, G. Aurégan, P. Hantraye, E. Brouillet, L. Buée, M. Colin,
914 Ectosomes: a new mechanism for non-exosomal secretion of tau protein, PLoS One 9(6) (2014)
915 e100760.
916 [32] V. Budnik, C. Ruiz-Cañada, F. Wendler, Extracellular vesicles round off communication in
917 the nervous system, Nat Rev Neurosci 17(3) (2016) 160-72.
918 [33] B. Combs, C.T. Tiernan, C. Hamel, N.M. Kanaan, Production of recombinant tau oligomers
919 in vitro, Methods Cell Biol 141 (2017) 45-64.
920 [34] L.A. Mulcahy, R.C. Pink, D.R. Carter, Routes and mechanisms of extracellular vesicle
921 uptake, J Extracell Vesicles 3 (2014).
922 [35] A.E. Morelli, A.T. Larregina, W.J. Shufesky, M.L. Sullivan, D.B. Stolz, G.D. Papworth,
923 A.F. Zahorchak, A.J. Logar, Z. Wang, S.C. Watkins, L.D. Falo, Jr., A.W. Thomson,
924 Endocytosis, intracellular sorting, and processing of exosomes by dendritic cells, Blood 104(10)
925 (2004) 3257-66.
926 [36] B.H. Sung, T. Ketova, D. Hoshino, A. Zijlstra, A.M. Weaver, Directional cell movement
927 through tissues is controlled by exosome secretion, Nature communications 6 (2015) 7164.
928 [37] A. Purushothaman, S.K. Bandari, J. Liu, J.A. Mobley, E.E. Brown, R.D. Sanderson,
929 Fibronectin on the Surface of Myeloma Cell-derived Exosomes Mediates Exosome-Cell
930 Interactions, J Biol Chem 291(4) (2016) 1652-63.

931 [38] H.C. Christianson, K.J. Svensson, T.H. van Kuppevelt, J.P. Li, M. Belting, Cancer cell
932 exosomes depend on cell-surface heparan sulfate proteoglycans for their internalization and
933 functional activity, Proc Natl Acad Sci U S A 110(43) (2013) 17380-5.
934 [39] C. Barres, L. Blanc, P. Bette-Bobillo, S. Andre, R. Mamoun, H.J. Gabius, M. Vidal,
935 Galectin-5 is bound onto the surface of rat reticulocyte exosomes and modulates vesicle uptake
936 by macrophages, Blood 115(3) (2010) 696-705.
937 [40] H. Im, H. Shao, Y.I. Park, V.M. Peterson, C.M. Castro, R. Weissleder, H. Lee, Label-free
938 detection and molecular profiling of exosomes with a nano-plasmonic sensor, Nat Biotechnol
939 32(5) (2014) 490-5.
940 [41] J.W. Kinney, S.M. Bemiller, A.S. Murtishaw, A.M. Leisgang, A.M. Salazar, B.T. Lamb,
941 Inflammation as a central mechanism in Alzheimer's disease, Alzheimers Dement (N Y) 4
942 (2018) 575-590.
943 [42] B.B. Holmes, J.L. Furman, T.E. Mahan, T.R. Yamasaki, H. Mirbaha, W.C. Eades, L.
944 Belaygorod, N.J. Cairns, D.M. Holtzman, M.I. Diamond, Proteopathic tau seeding predicts
945 tauopathy in vivo, Proc Natl Acad Sci U S A 111(41) (2014) E4376-85.
946 [43] K. Blennow, A. Wallin, H. Agren, C. Spenger, J. Siegfried, E. Vanmechelen, Tau protein in
947 cerebrospinal fluid: a biochemical marker for axonal degeneration in Alzheimer disease?, Mol
948 Chem Neuropathol 26(3) (1995) 231-45.
949 [44] E.M. Sigurdsson, Tau Immunotherapies for Alzheimer's Disease and Related Tauopathies:
950 Progress and Potential Pitfalls, J Alzheimers Dis 66(2) (2018) 855-856.
951 [45] W. Zhang, A. Tarutani, K.L. Newell, A.G. Murzin, T. Matsubara, B. Falcon, R. Vidal, H.J.
952 Garringer, Y. Shi, T. Ikeuchi, S. Murayama, B. Ghetti, M. Hasegawa, M. Goedert, S.H.W.
953 Scheres, Novel tau filament fold in corticobasal degeneration, Nature (2020).

954 [46] B. Falcon, J. Zivanov, W. Zhang, A.G. Murzin, H.J. Garringer, R. Vidal, R.A. Crowther,
955 K.L. Newell, B. Ghetti, M. Goedert, S.H.W. Scheres, Novel tau filament fold in chronic
956 traumatic encephalopathy encloses hydrophobic molecules, Nature 568(7752) (2019) 420-423.
957 [47] B. Falcon, W. Zhang, A.G. Murzin, G. Murshudov, H.J. Garringer, R. Vidal, R.A.
958 Crowther, B. Ghetti, S.H.W. Scheres, M. Goedert, Structures of filaments from Pick's disease
959 reveal a novel tau protein fold, Nature 561(7721) (2018) 137-140.
960 [48] A.W.P. Fitzpatrick, B. Falcon, S. He, A.G. Murzin, G. Murshudov, H.J. Garringer, R.A.
961 Crowther, B. Ghetti, M. Goedert, S.H.W. Scheres, Cryo-EM structures of tau filaments from
962 Alzheimer's disease, Nature 547(7662) (2017) 185-190.
963 [49] L. Jiang, P.E.A. Ash, B.F. Maziuk, H.I. Ballance, S. Boudeau, A.A. Abdullatif, M. Orlando,
964 L. Petrucelli, T. Ikezu, B. Wolozin, TIA1 regulates the generation and response to toxic tau
965 oligomers, Acta Neuropathol 137(2) (2019) 259-277.
966 [50] D.J. Apicco, P.E.A. Ash, B. Maziuk, C. LeBlang, M. Medalla, A. Al Abdullatif, A.
967 Ferragud, E. Botelho, H.I. Ballance, U. Dhawan, S. Boudeau, A.L. Cruz, D. Kashy, A. Wong,
968 L.R. Goldberg, N. Yazdani, C. Zhang, C.Y. Ung, Y. Tripodis, N.M. Kanaan, T. Ikezu, P.
969 Cottone, J. Leszyk, H. Li, J. Luebke, C.D. Bryant, B. Wolozin, Reducing the RNA binding
970 protein TIA1 protects against tau-mediated neurodegeneration in vivo, Nat Neurosci 21(1)
971 (2018) 72-80.
972 [51] G. Ghag, N. Bhatt, D.V. Cantu, M.J. Guerrero-Munoz, A. Ellsworth, U. Sengupta, R.
973 Kayed, Soluble tau aggregates, not large fibrils, are the toxic species that display seeding and
974 cross-seeding behavior, Protein Sci 27(11) (2018) 1901-1909.
975 [52] A. Hoshino, B. Costa-Silva, T.L. Shen, G. Rodrigues, A. Hashimoto, M. Tesic Mark, H.
976 Molina, S. Kohsaka, A. Di Giannatale, S. Ceder, S. Singh, C. Williams, N. Soplop, K. Uryu, L.

977 Pharmer, T. King, L. Bojmar, A.E. Davies, Y. Ararso, T. Zhang, H. Zhang, J. Hernandez, J.M.
978 Weiss, V.D. Dumont-Cole, K. Kramer, L.H. Wexler, A. Narendran, G.K. Schwartz, J.H. Healey,
979 P. Sandstrom, K.J. Labori, E.H. Kure, P.M. Grandgenett, M.A. Hollingsworth, M. de Sousa, S.
980 Kaur, M. Jain, K. Mallya, S.K. Batra, W.R. Jarnagin, M.S. Brady, O. Fodstad, V. Muller, K.
981 Pantel, A.J. Minn, M.J. Bissell, B.A. Garcia, Y. Kang, V.K. Rajasekhar, C.M. Ghajar, I. Matei,
982 H. Peinado, J. Bromberg, D. Lyden, Tumour exosome integrins determine organotropic
983 metastasis, Nature 527(7578) (2015) 329-35.
984 [53] I. Nazarenko, S. Rana, A. Baumann, J. McAlear, A. Hellwig, M. Trendelenburg, G. Lochnit,
985 K.T. Preissner, M. Zoller, Cell surface tetraspanin Tspan8 contributes to molecular pathways of
986 exosome-induced endothelial cell activation, Cancer Res 70(4) (2010) 1668-78.
987 [54] F. Volz, H.H. Bock, M. Gierthmuehlen, J. Zentner, C.A. Haas, T.M. Freiman, Stereologic
988 estimation of hippocampal GluR2/3- and calretinin-immunoreactive hilar neurons (presumptive
989 mossy cells) in two mouse models of temporal lobe epilepsy, Epilepsia 52(9) (2011) 1579-89.
990 [55] R. Zimmer, A.W. Teelken, W.B. Trieling, W. Weber, T. Weihmayr, H. Lauter, Gamma-
991 aminobutyric acid and homovanillic acid concentration in the CSF of patients with senile
992 dementia of Alzheimer's type, Arch Neurol 41(6) (1984) 602-4.
993 [56] S.R. Bareggi, M. Franceschi, L. Bonini, L. Zecca, S. Smirne, Decreased CSF concentrations
994 of homovanillic acid and gamma-aminobutyric acid in Alzheimer's disease. Age- or disease-
995 related modifications?, Arch Neurol 39(11) (1982) 709-12.
996 [57] K. Govindpani, B. Calvo-Flores Guzman, C. Vinnakota, H.J. Waldvogel, R.L. Faull, A.
997 Kwakowsky, Towards a Better Understanding of GABAergic Remodeling in Alzheimer's
998 Disease, Int J Mol Sci 18(8) (2017).

999 [58] V. Chan-Palay, Somatostatin immunoreactive neurons in the human hippocampus and
1000 cortex shown by immunogold/silver intensification on vibratome sections: coexistence with
1001 neuropeptide Y neurons, and effects in Alzheimer-type dementia, J Comp Neurol 260(2) (1987)
1002 201-23.
1003 [59] P. Davies, R. Katzman, R.D. Terry, Reduced somatostatin-like immunoreactivity in cerebral
1004 cortex from cases of Alzheimer disease and Alzheimer senile dementa, Nature 288(5788) (1980)
1005 279-80.
1006 [60] J.J. Palop, L. Mucke, Epilepsy and cognitive impairments in Alzheimer disease, Arch
1007 Neurol 66(4) (2009) 435-40.
1008 [61] M.R. Schoenberg, R.S. Rum, K.E. Osborn, M.A. Werz, A randomized, double-blind,
1009 placebo-controlled crossover study of the effects of levetiracetam on cognition, mood, and
1010 balance in healthy older adults, Epilepsia 58(9) (2017) 1566-1574.
1011 [62] K.A. Vossel, A.J. Beagle, G.D. Rabinovici, H. Shu, S.E. Lee, G. Naasan, M. Hegde, S.B.
1012 Cornes, M.L. Henry, A.B. Nelson, W.W. Seeley, M.D. Geschwind, M.L. Gorno-Tempini, T.
1013 Shih, H.E. Kirsch, P.A. Garcia, B.L. Miller, L. Mucke, Seizures and epileptiform activity in the
1014 early stages of Alzheimer disease, JAMA neurology 70(9) (2013) 1158-66.
1015 [63] R.J. Hatch, Y. Wei, D. Xia, J. Gotz, Hyperphosphorylated tau causes reduced hippocampal
1016 CA1 excitability by relocating the axon initial segment, Acta Neuropathologica 133(5) (2017)
1017 717-730.
1018 [64] L. Cheng, J.D. Doecke, R.A. Sharples, V.L. Villemagne, C.J. Fowler, A. Rembach, R.N.
1019 Martins, C.C. Rowe, S.L. Macaulay, C.L. Masters, A.F. Hill, B. Australian Imaging, G. Lifestyle
1020 Research, Prognostic serum miRNA biomarkers associated with Alzheimer's disease shows

1021 concordance with neuropsychological and neuroimaging assessment, Mol Psychiatry 20(10)
1022 (2015) 1188-96.
1023 [65] R.A. Stern, Y. Tripodis, C.M. Baugh, N.G. Fritts, B.M. Martin, C. Chaisson, R.C. Cantu,
1024 J.A. Joyce, S. Shah, T. Ikezu, J. Zhang, C. Gercel-Taylor, D.D. Taylor, Preliminary Study of
1025 Plasma Exosomal Tau as a Potential Biomarker for Chronic Traumatic Encephalopathy, J
1026 Alzheimers Dis (2016).
1027 [66] K.M. McAvoy, H. Rajamohamed Sait, G. Marsh, M. Peterson, T.L. Reynolds, J. Gagnon, S.
1028 Geisler, P. Leach, C. Roberts, E. Cahir-McFarland, R.M. Ransohoff, A. Crotti, Cell-autonomous
1029 and non-cell autonomous effects of neuronal BIN1 loss in vivo, PLoS One 14(8) (2019)
1030 e0220125.
1031 [67] H. Mathys, J. Davila-Velderrain, Z. Peng, F. Gao, S. Mohammadi, J.Z. Young, M. Menon,
1032 L. He, F. Abdurrob, X. Jiang, A.J. Martorell, R.M. Ransohoff, B.P. Hafler, D.A. Bennett, M.
1033 Kellis, L.H. Tsai, Single-cell transcriptomic analysis of Alzheimer's disease, Nature 570(7761)
1034 (2019) 332-337.
1035 [68] J.C. Lambert, S. Heath, G. Even, D. Campion, K. Sleegers, M. Hiltunen, O. Combarros, D.
1036 Zelenika, M.J. Bullido, B. Tavernier, L. Letenneur, K. Bettens, C. Berr, F. Pasquier, N. Fievet, P.
1037 Barberger-Gateau, S. Engelborghs, P. De Deyn, I. Mateo, A. Franck, S. Helisalmi, E. Porcellini,
1038 O. Hanon, M.M. de Pancorbo, C. Lendon, C. Dufouil, C. Jaillard, T. Leveillard, V. Alvarez, P.
1039 Bosco, M. Mancuso, F. Panza, B. Nacmias, P. Bossu, P. Piccardi, G. Annoni, D. Seripa, D.
1040 Galimberti, D. Hannequin, F. Licastro, H. Soininen, K. Ritchie, H. Blanche, J.F. Dartigues, C.
1041 Tzourio, I. Gut, C. Van Broeckhoven, A. Alperovitch, M. Lathrop, P. Amouyel, Genome-wide
1042 association study identifies variants at CLU and CR1 associated with Alzheimer's disease, Nat
1043 Genet 41(10) (2009) 1094-9.

1044 [69] S. Krasemann, C. Madore, R. Cialic, C. Baufeld, N. Calcagno, R. El Fatimy, L. Beckers, E.
1045 O'Loughlin, Y. Xu, Z. Fanek, D.J. Greco, S.T. Smith, G. Tweet, Z. Humulock, T. Zrzavy, P.
1046 Conde-Sanroman, M. Gacias, Z. Weng, H. Chen, E. Tjon, F. Mazaheri, K. Hartmann, A. Madi,
1047 J.D. Ulrich, M. Glatzel, A. Worthmann, J. Heeren, B. Budnik, C. Lemere, T. Ikezu, F.L.
1048 Heppner, V. Litvak, D.M. Holtzman, H. Lassmann, H.L. Weiner, J. Ochando, C. Haass, O.
1049 Butovsky, The TREM2-APOE Pathway Drives the Transcriptional Phenotype of Dysfunctional
1050 Microglia in Neurodegenerative Diseases, Immunity 47(3) (2017) 566-581 e9.
1051 [70] T. Quast, F. Eppler, V. Semmling, C. Schild, Y. Homsi, S. Levy, T. Lang, C. Kurts, W.
1052 Kolanus, CD81 is essential for the formation of membrane protrusions and regulates Rac1-
1053 activation in adhesion-dependent immune cell migration, Blood 118(7) (2011) 1818-27.
1054 [71] B. He, L. Liu, G.A. Cook, S. Grgurevich, L.K. Jennings, X.A. Zhang, Tetraspanin CD82
1055 attenuates cellular morphogenesis through down-regulating integrin alpha6-mediated cell
1056 adhesion, J Biol Chem 280(5) (2005) 3346-54.
1057 [72] J. Levenga, P. Krishnamurthy, H. Rajamohamedsait, H. Wong, T.F. Franke, P. Cain, E.M.
1058 Sigurdsson, C.A. Hoeffer, Tau pathology induces loss of GABAergic interneurons leading to
1059 altered synaptic plasticity and behavioral impairments, Acta Neuropathol Commun 1 (2013) 34.
1060 [73] H. Soler, J. Dorca-Arevalo, M. Gonzalez, S.E. Rubio, J. Avila, E. Soriano, M. Pascual, The
1061 GABAergic septohippocampal connection is impaired in a mouse model of tauopathy, Neurobiol
1062 Aging 49 (2017) 40-51.
1063 [74] S.S. Deepa, D. Carulli, C. Galtrey, K. Rhodes, J. Fukuda, T. Mikami, K. Sugahara, J.W.
1064 Fawcett, Composition of perineuronal net extracellular matrix in rat brain: a different
1065 disaccharide composition for the net-associated proteoglycans, J Biol Chem 281(26) (2006)
1066 17789-800.

[75] S. Muraoka, M.P. Jedrychowski, H. Tatebe, A.M. DeLeo, S. Ikezu, T. Tokuda, S.P. Gygi, R.A. Stern, T. Ikezu, Proteomic Profiling of Extracellular Vesicles Isolated From Cerebrospinal Fluid of Former National Football League Players at Risk for Chronic Traumatic Encephalopathy, Front Neurosci 13 (2019) 1059.

[76] U. Sengupta, M. Carretero-Murillo, R. Kayed, Preparation and Characterization of Tau Oligomer Strains, Methods Mol Biol 1779 (2018) 113-146.

Figure 1. Characterization of EVs using dot blot with multiple Tau oligomer antibodies, and Atomic force microscopy

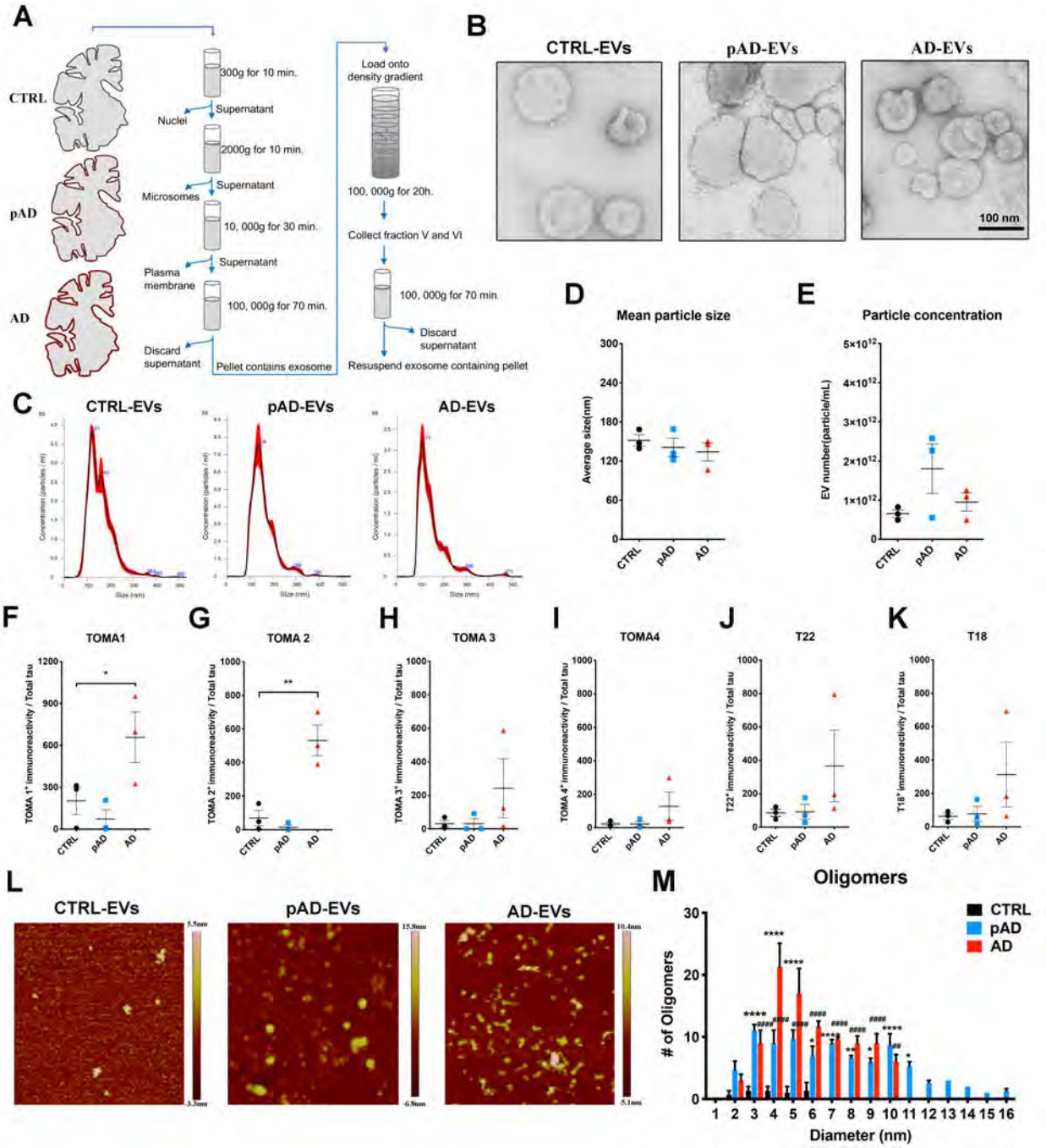

Figure 2. EV-tau derived from AD brain was taken up by cultured neurons more efficiently

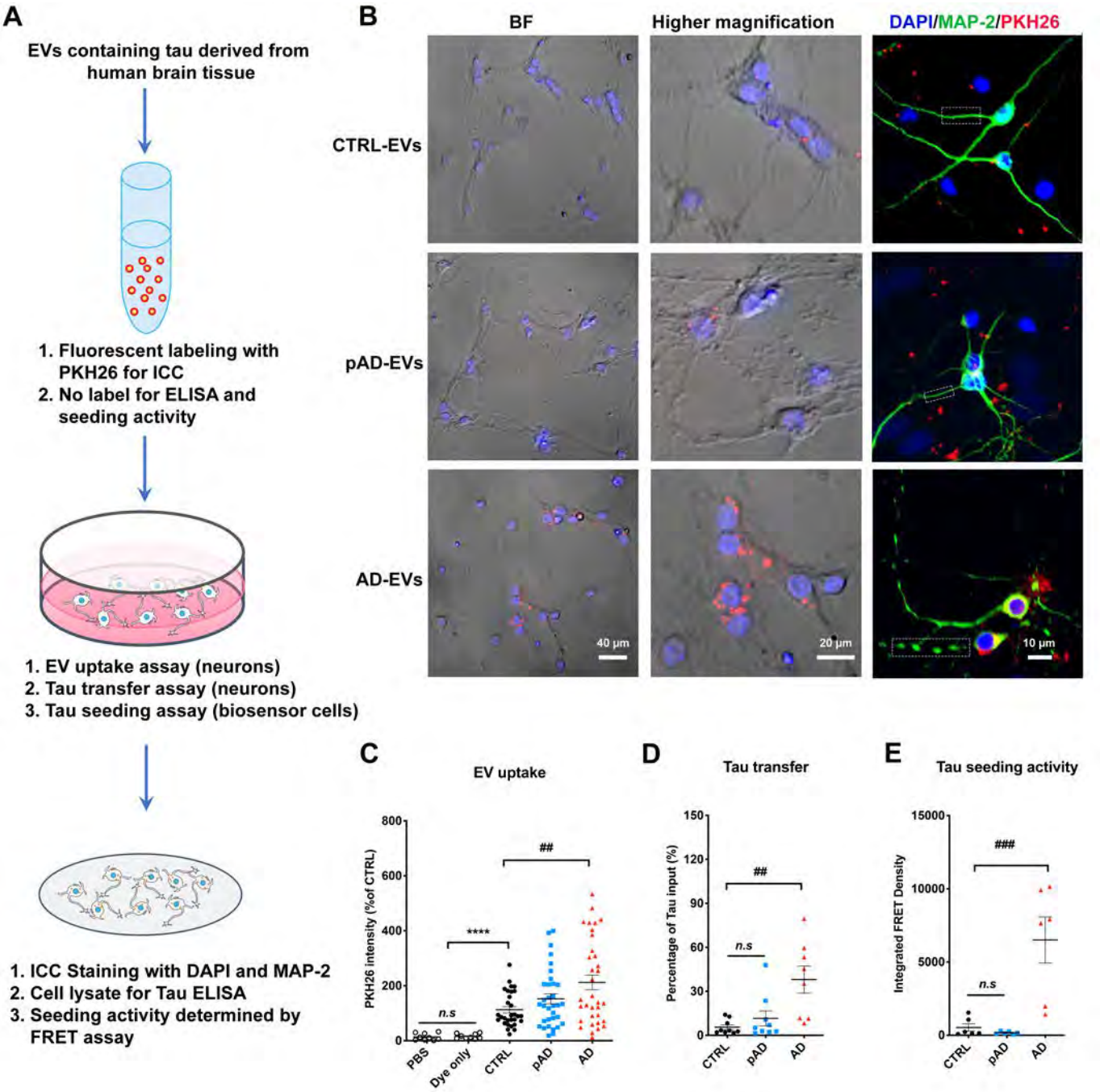

Figure 3. AD and pAD brain derived exosome but not CTRL injection causes progressive tauopathy in C57BL/6 mice AT8 staining

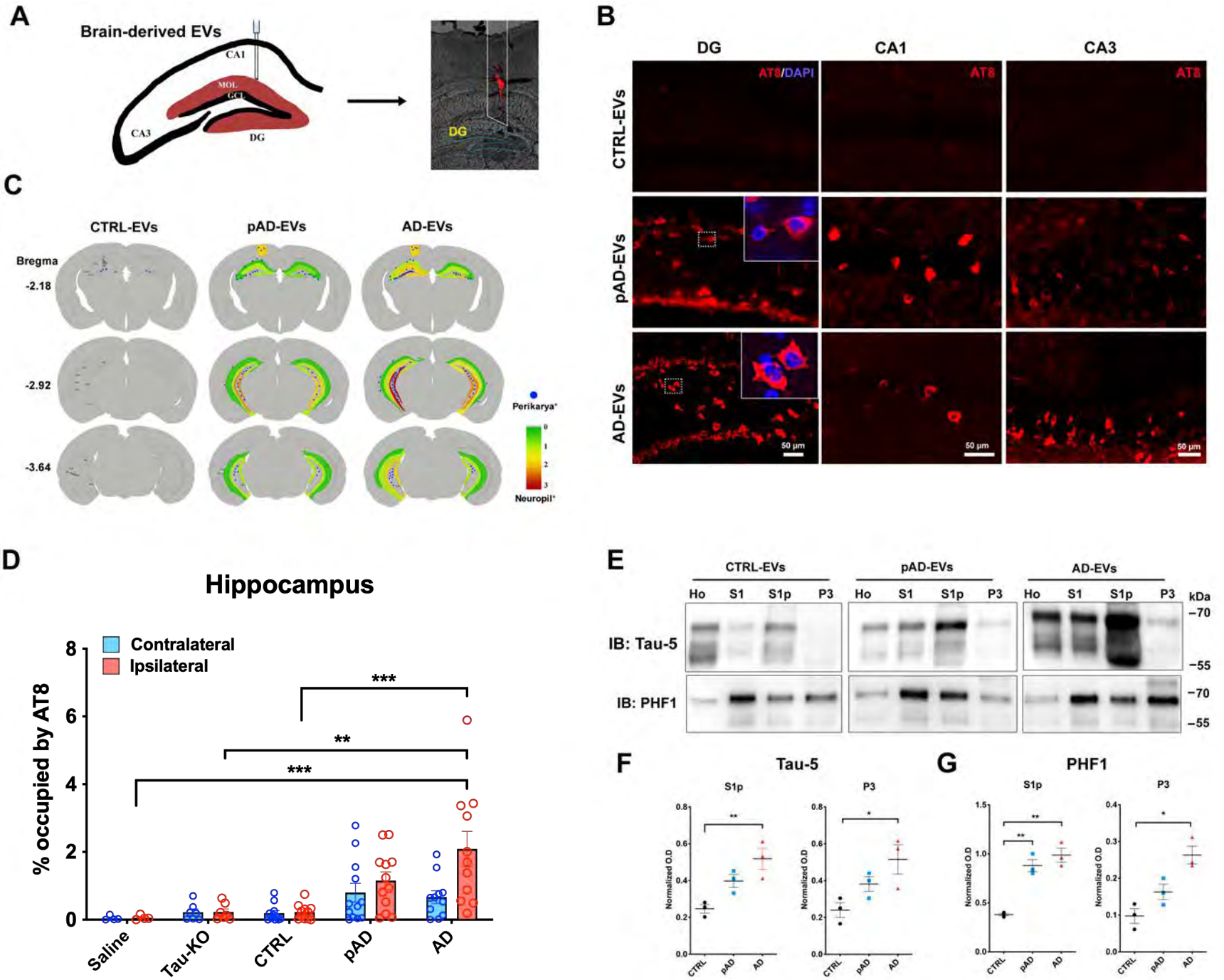

Figure 4. Limit amount of EV-tau not oligomeric or fibril tau derived from AD brain induced tau propagation in mouse brain

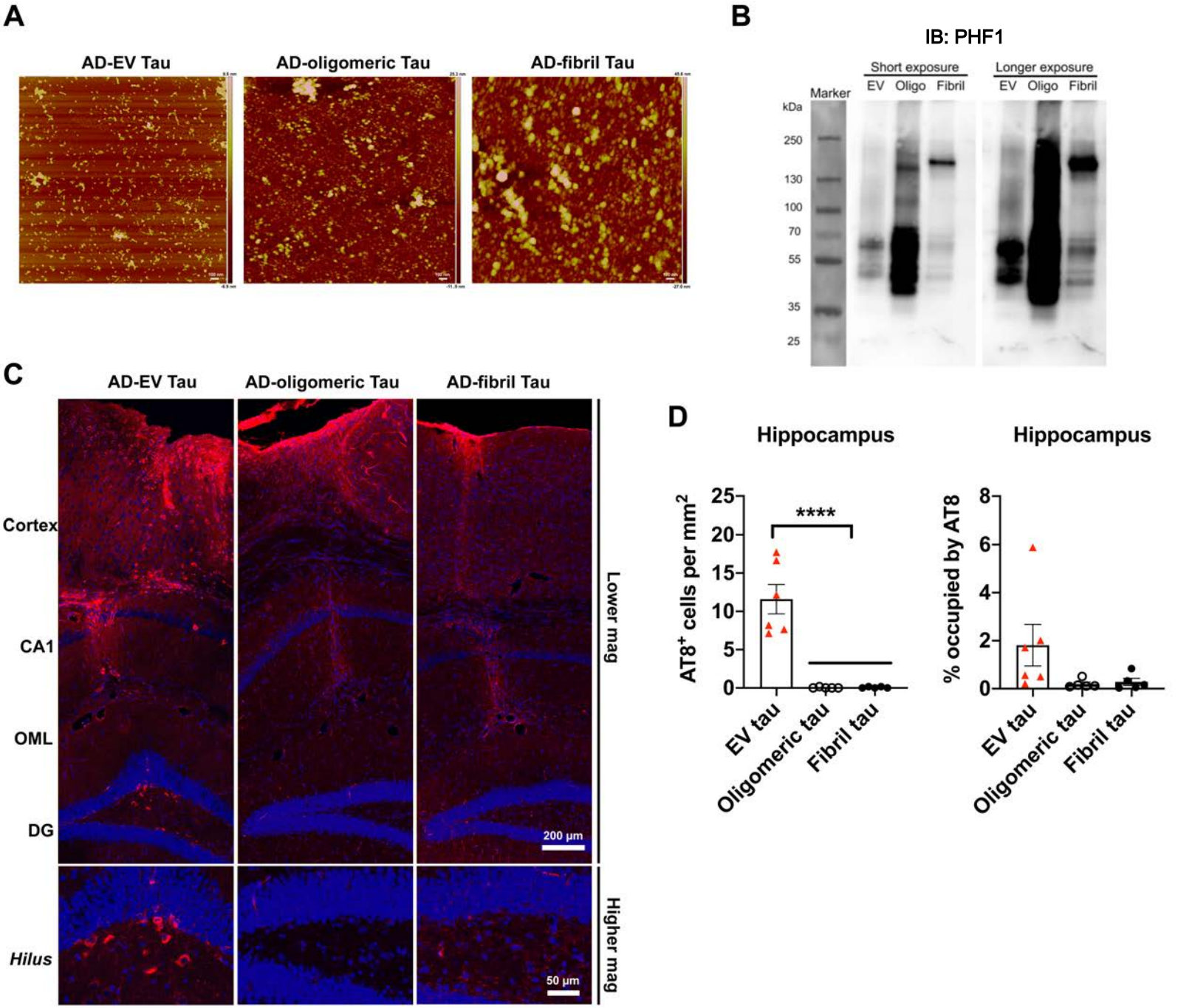

Figure 5. Co-localization of pathological tau staining with AT8 antibody in GABAergic interneurons in the hippocampus of C57BL/6 mice

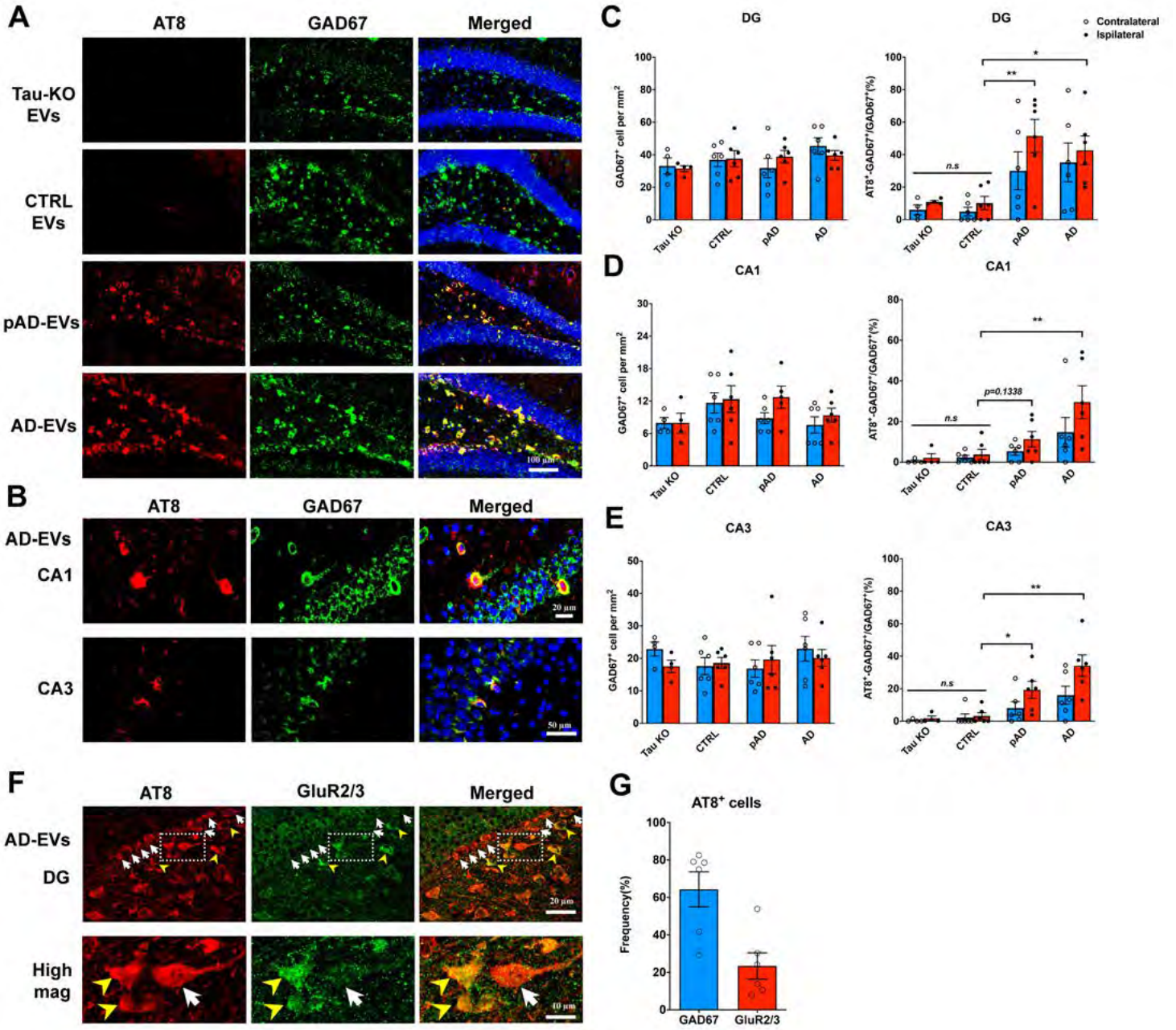

Figure 6. AD-EV and pAD-EV inoculation reduced GABAergic input and neuronal activity in CA1 pyramidal cells.

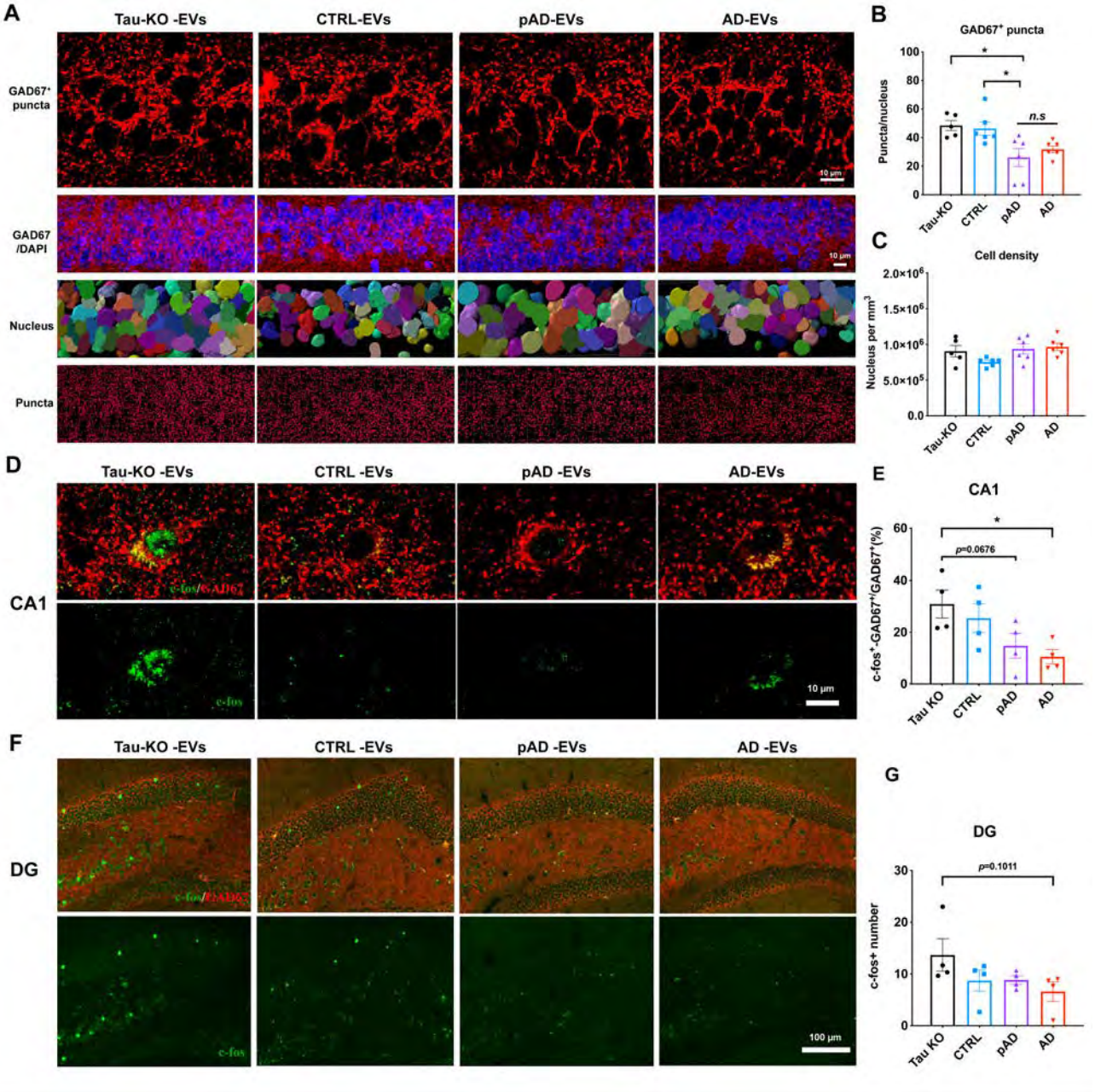

Figure 7. Mouse CA1 pyramidal neurons exhibit clear cellular morphology after biocytin filling which was patched clamp by using patch pipette.

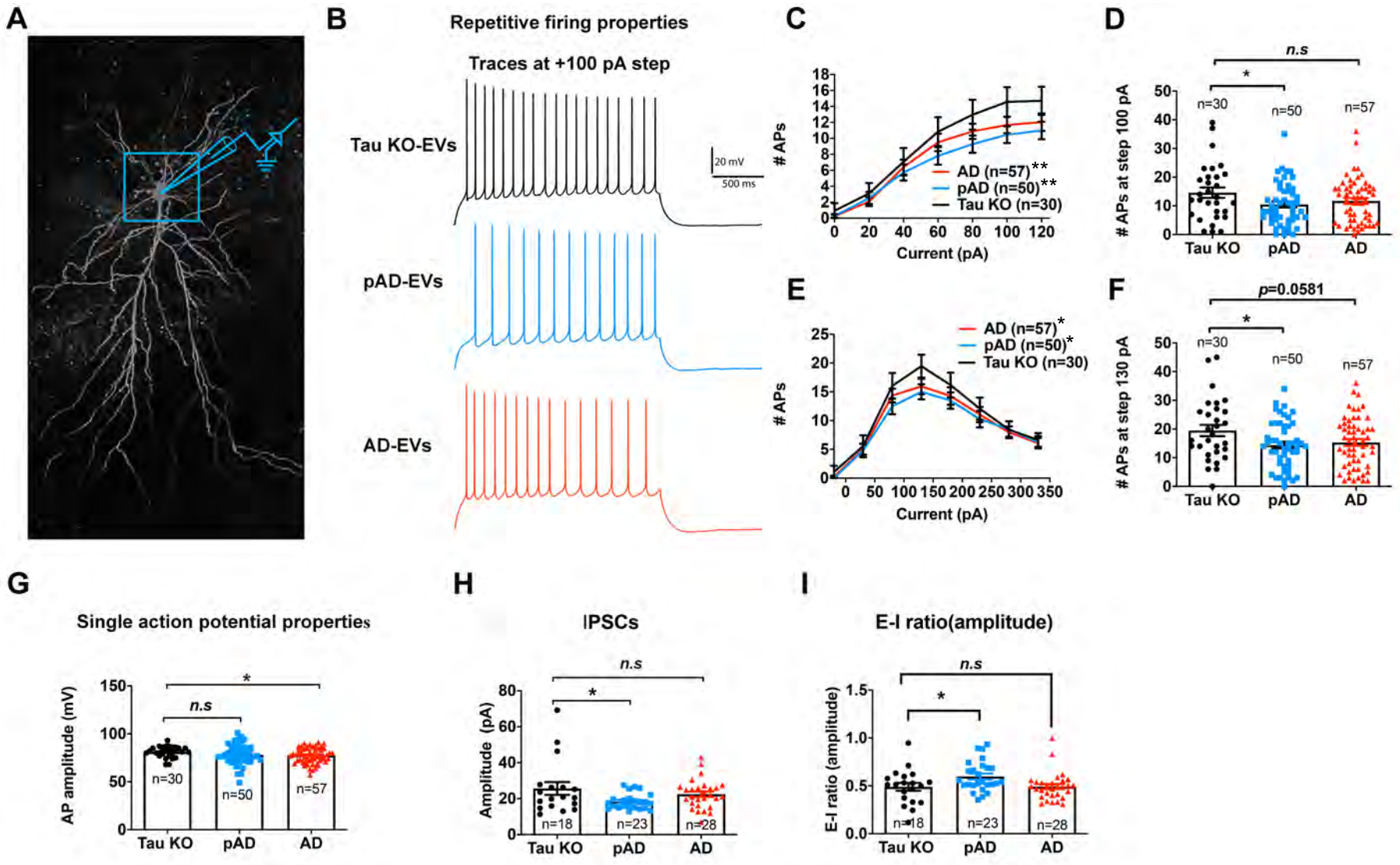

Supplemental Figure S1. Dot blot of EVs sample with multiple tau oligomer antibodies

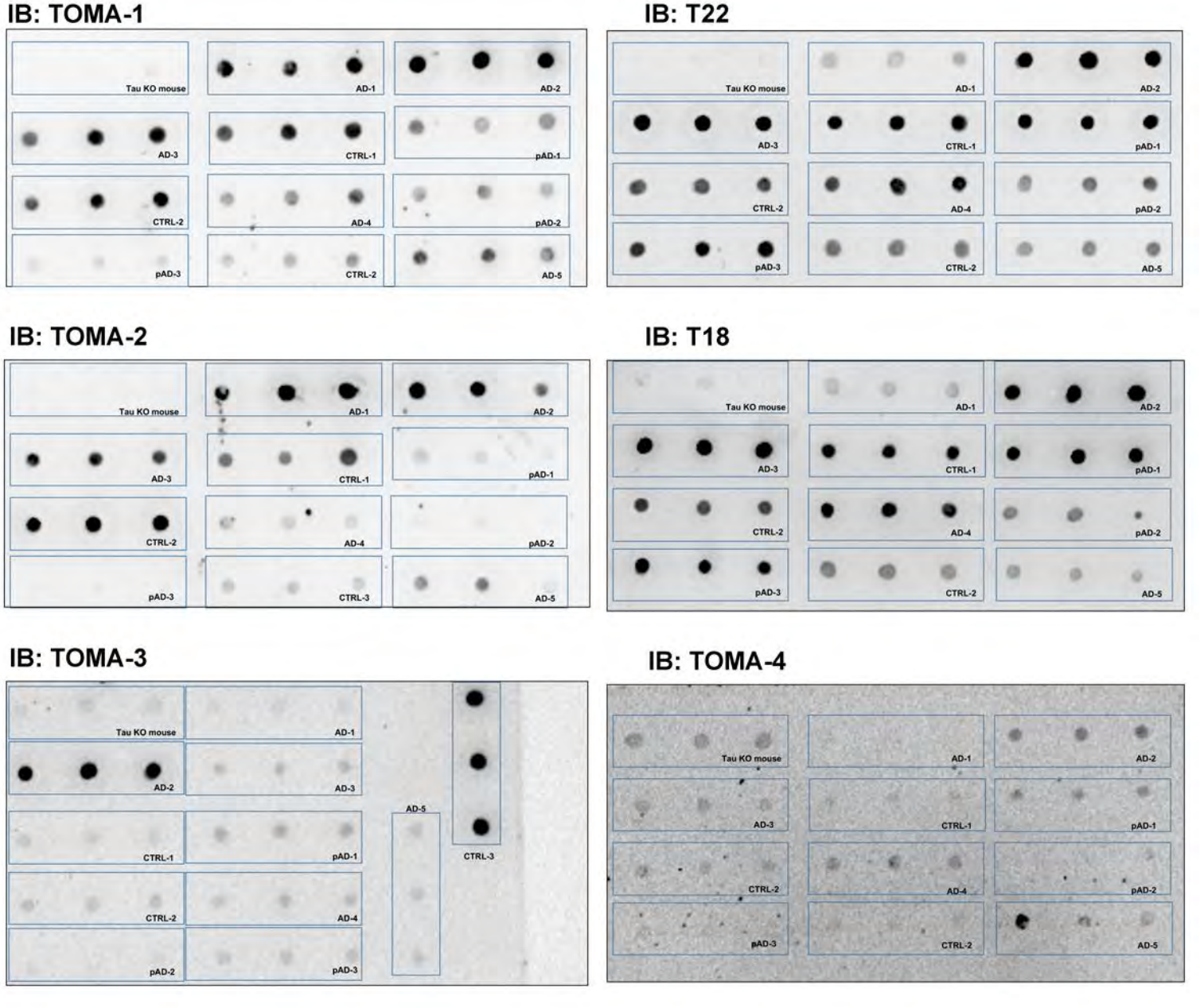

Supplemental Figure S2. AT8 staining showed Tau pathology of young mice and aged mice were injected of EVs derived from human brain

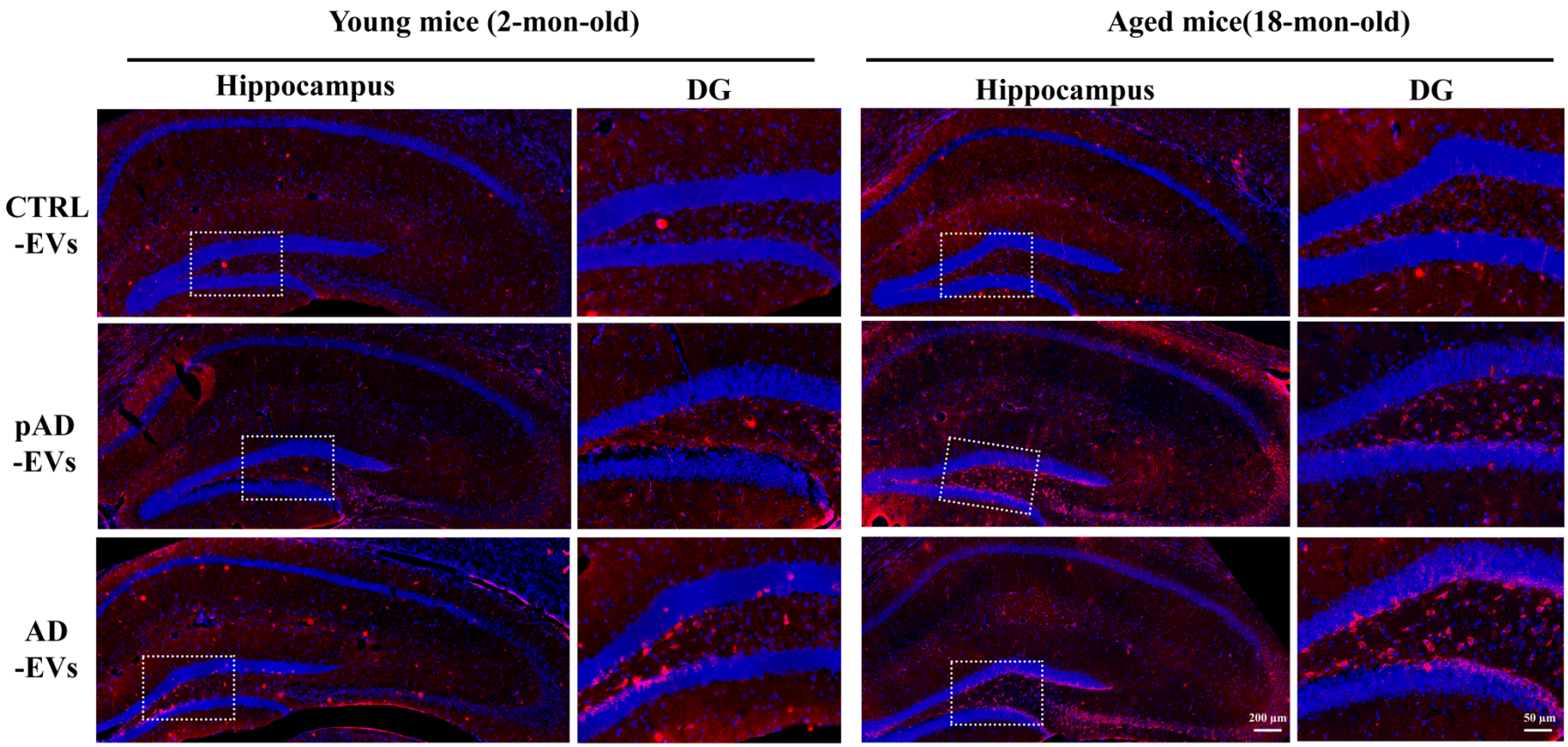

Supplemental Figure S3. Tau pathology staining with Alz50, MC1, CP13, PS422 and PHF1 antibodies

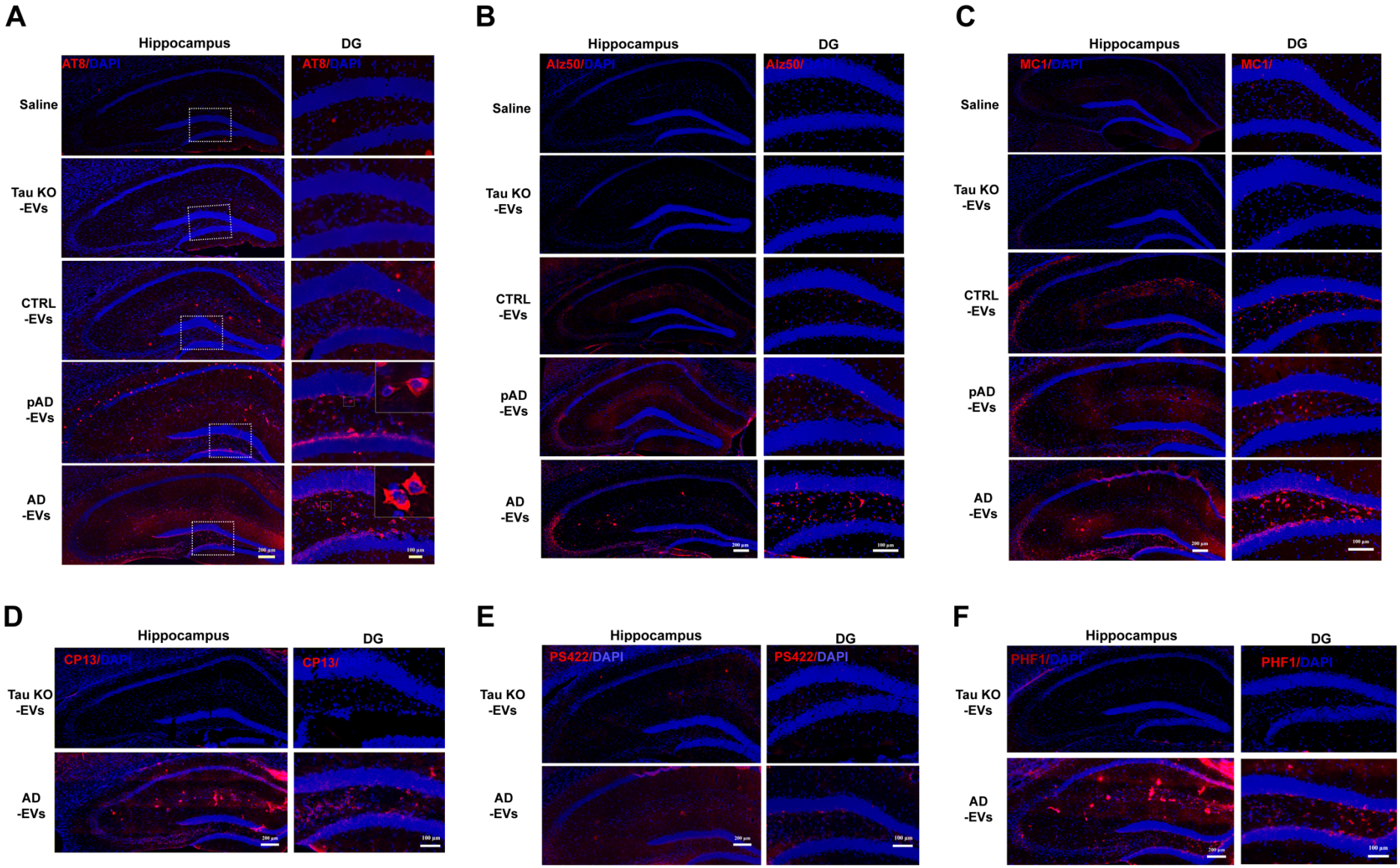

Supplemental Figure S4. Lateral spread of p-Tau in the injection site of cortex

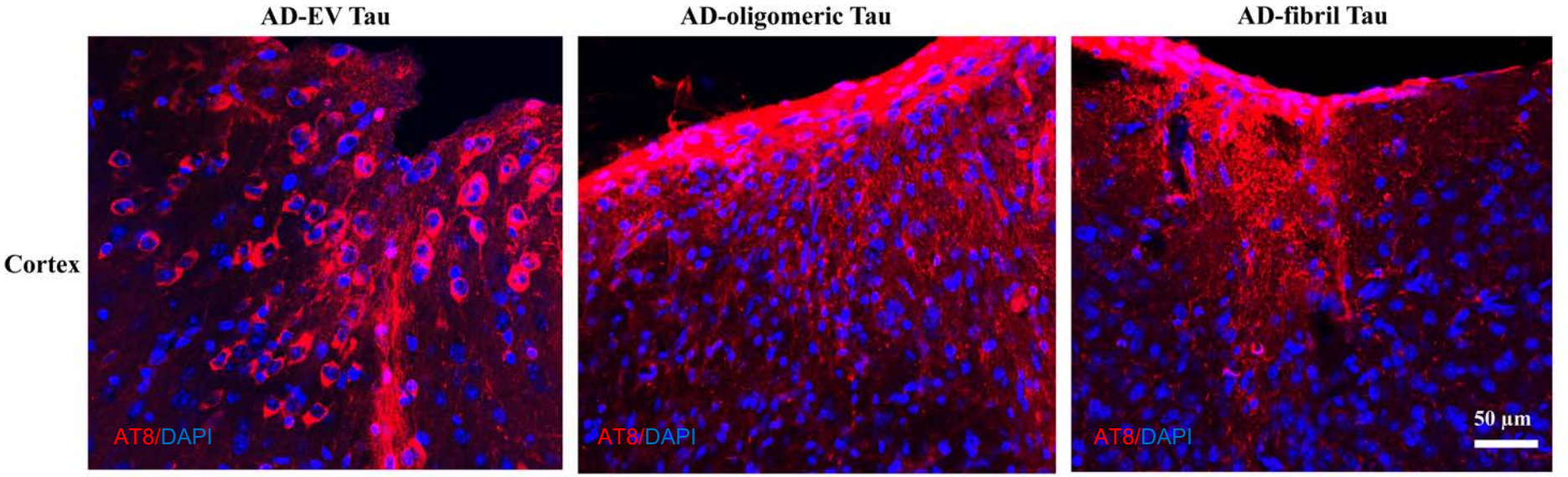
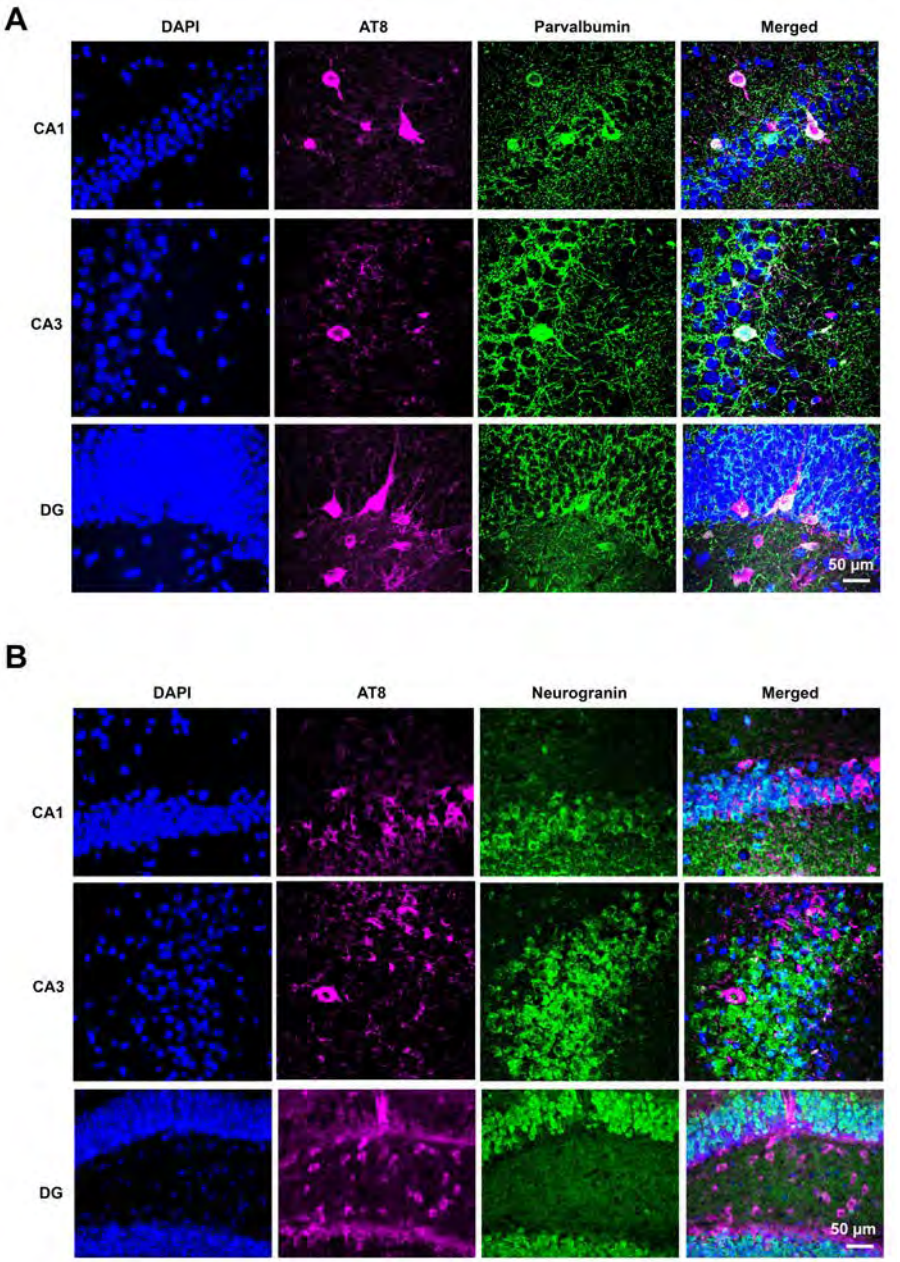
Supplemental Figure S5. AT8^{+} cell were co-stained with parvalbumin but not neurogranin